AD-A185 885

CUMENTATION PAGE

1a. REPORT SECURITY CLASSIFICATION UNCLASSIFIED		1b. RESTRICTIVE MARKINGS			
2a. SECURITY CLASSIFICATION AUTHORITY		3. DISTRIBUTION/AVAILABILITY OF REPORT Approved for public release; distribution unlimited.			
2b. DECLASSIFICATION/DOWNGRADING SCHEDULE					
4. PERFORMING ORGANIZATION REPORT NUMBER(S)		5. MONITORING ORGANIZATION REPORT NUMBER(S) AFOSR-TR. 87-1166			
6a. NAME OF PERFORMING ORGANIZATION Schwartz Electro-Optics Boston Division	6b. OFFICE SYMBOL (If applicable) SEO	7a. NAME OF MONITORING ORGANIZATION AFOSR			
6c. ADDRESS (City, State and ZIP Code) 45 Winthrop Street Concord, MA 01742		7b. ADDRESS (City, State and ZIP Code) Building 410 Bolling AFB DC 20332-6448			
8a. NAME OF FUNDING/SPONSORING ORGANIZATION USAF, AFSC (AFOSR)	8b. OFFICE SYMBOL (If applicable) NP	9. PROCUREMENT INSTRUMENT IDENTIFICATION NUMBER F 49620-86-C-0074			
8c. ADDRESS (City, State and ZIP Code) Building 410 Bolling AFB DC 20332-6448		10. SOURCE OF FUNDING NOS.			

		PROGRAM ELEMENT NO.	PROJECT NO.	TASK NO.	WORK UNIT NO.
		61102F	2301	A1	

11. TITLE (Include Security Classification)
Characterization of Er,Cr:YSGG (U)

12. PERSONAL AUTHOR(S)
Moulton, Peter Franklin

13a. TYPE OF REPORT Final	13b. TIME COVERED FROM 07/1/86 TO 12/31/86	14. DATE OF REPORT (Yr., Mo., Day) 87 June 3	15. PAGE COUNT 35

16. SUPPLEMENTARY NOTATION

17	COSATI CODES		18. SUBJECT TERMS (Continue on reverse if necessary and identify by block number)
FIELD	GROUP	SUB. GR.	Lasers, Solid State, 2800-nm Lasers, Erbium Doped

19. ABSTRACT (Continue on reverse if necessary and identify by block number)

A study of the spectroscopic and laser properties of the crystal erbium-and chromium-doped yttrium scandium gallium garnet (Er,Cr:YSGG) has been carried out. The absorption spectra from 300-1700 nm and the emission spectra in the regions around 800,1600 and 2800 nm have been measured, along with the kinetics of emission and decay under pulsed excitation. Energy levels of the erbium ion have been determined. Analysis of the data shows that energy transfers from excited chromium ions to erbium ions with near-100% efficiency. The 2800-nm-region laser performance of Er,Cr:YSGG, under flashlamp pumping conditions has been observed and found to be superior in some aspects to other erbium-doped crystals.

87 082

20. DISTRIBUTION/AVAILABILITY OF ABSTRACT UNCLASSIFIED/UNLIMITED ☐ SAME AS RPT ☐ DTIC USERS ☐	21. ABSTRACT SECURITY CLASSIFICATION unclassified	
22a. NAME OF RESPONSIBLE INDIVIDUAL Dr Howard R. Schlossberg	22b. TELEPHONE NUMBER (Include Area Code) 202/767-4906	22c. OFFICE SYMBOL NP

DD FORM 1473, 83 APR   EDITION OF 1 JAN 73 IS OBSOLETE.   UNCLASSIFIED

Final Report:

Characterization of Er,Cr:YSGG

Contract: F49620-86-C-0074

Reporting Period: 1 July 1986 - 31 December 1986

Submitted by:
Schwartz Electro-Optics, Inc.
Boston Division
45 Winthrop Street
Concord, MA 01742

Accesion For		
NTIS CRA&I		
DTIC TAB	☐	
Unannounced	☐	
Justification		
By		
Distribution		
Availability Codes		
Dist	Avail and / or Special	
A-1		

1 Introduction

One research activity of continuing interest in the general area of solid state lasers involves studies to increase the efficiency of lamp-pumped systems in converting lamp input power to laser output power. Under some circumstances dopant ions (or 'sensitizers'), different from the laser-active ion, can be added to a laser crystal to absorb additional energy from the pumping source and nonradiatively transfer excitation over to the active ion. If the sensitizer ion induces broad, intense absorption bands in the crystal then there can be a significant increase in pumping efficiency and, ultimately, laser efficiency. Current active efforts include the study of chromium-sensitized, rare-earth-doped, garnet-structured crystals, of which the most well-known is Nd^{3+}- and Er^{3+}-doped $Gd_3Sc_2Ga_3O_{12}$, or Nd,Cr:GSGG. Improvements in efficiency by nearly a factor of two over the most common solid state laser, $Nd:Y_3Al_5O_{12}$ (YAG), have been observed in flashlamp-pumped operation of the Nd,Cr:GSGG laser.[1-3]

The use of the Cr^{3+} ion as a sensitizer is desirable because the ion has two broad absorption bands in the red and blue-green wavelength regions, resulting from vibronic transitions to the $^4T_2$ and $^4T_1$ energy levels. The broad bands overlap well with the continuum emission from typical xenon flashlamps. Sensitization of Nd^{3+} by Cr^{3+} has been demonstrated[4] as far back as 1964 in the host garnet YAG, but the effectiveness of sensitization in YAG is limited because transfer from Cr^{3+} to Nd^{3+} is via the $^2E \rightarrow \, ^4A_2$ transition of Cr^{3+}, which is spin-forbidden and narrow in linewidth. These properties are not conducive to efficient transfer, because the matrix element for transfer (and, hence, the transfer rate) is proportional to the radiative dipole moment for the sensitizer ion and the overlap integral between the emission line of the sensitizer and the absorption lines of the active ion. Another problem with Cr^{3+} sensitization of YAG is the relatively poor acceptance of the Cr^{3+} ion in the host crystal, which puts a practical upper level on the concentration of sensitizers allowed without a significant degradation in crystal quality.

The effectiveness of Cr^{3+}-sensitization in GSGG and similar garnets results from two conditions, both of which are related to the relatively large lattice size of the garnets compared to YAG. First, the crystal field for the Cr^{3+} ion in the large-lattice garnets is low enough to place the $^4T_2$ excited-state energy level at roughly the same position as that of the ^2E level. Thus, the $^4T_2$ level is populated in the optical pumping process. Transitions to the ground state from the $^4T_2$ state are spin-allowed and spectrally broad, because of strong vibronic coupling, and thus excitation in the $^4T_2$ state has a relatively high transfer rate to the Nd^{3+} ion. Second, the large-lattice garnets like GSGG can accept concentrations of Cr^{3+} high enough to produce intense absorption bands in the crystal without compromising crystal quality. This is due to a good match in ionic radii between the Cr^{3+} ion and the ions for which Cr^{3+} substitutes.

There are laser-active trivalent rare-earth ions other than Nd^{3+} which can be sensitized by Cr^{3+}, including Er, Tm, and Ho (Ref. 5), and the large-lattice garnets as host crystals would be expected to provide conditions favorable to efficient sensitization. In fact, the improvement in efficiency afforded by Cr^{3+} sensitization for some of the rare-earth systems can be much more dramatic than that found for the Nd^{3+} lasers, since the three ions mentioned above have, compared to Nd^{3+}, relatively weak absorption cross sections and relatively few absorption bands at wavelengths overlapping the emission spectrum of typical flashlamps.

The Phase I proposal for the work to be discussed here addressed the study of one particular solid state system, Cr^{3+}-sensitized Er^{3+} in the GSGG host. The specific objectives of the Phase I effort were stated as follows:

a. Develop specifications for crystals and procure a crystal of GSGG with appropriate Er^{3+} and Cr^{3+} doping.
b. Study the crystal procurred in a. by absorption and fluorescence spectroscopy, emphasizing the Er^{3+} transitions at 1600 and 2900 nm.
c. Study, by fluorescence decay, the energy transfer rates and lifetimes of the excited states of the Er^{3+} and Cr^{3+} ions.

1

d. Use the data obtained from the above studies to determine optimum doping levels of Er³⁺ and Cr³⁺ in GSGG for lasing at 1600 and 2900 nm.
e. Attempt to obtain and study laser action from the Er,Cr:GSGG crystal if it is of sufficient quality.

At the time the proposal was written, there were reports that the Soviet research group responsible for the first demonstration of Nd,Cr:GSGG laser, led by I.A. Shcherbakov at the Institute of General Physics, had begun exploration other sensitized rare earth systems, including Er^{3+} (Ref. 6). In the period of time between the submission of the Phase I proposal and the start of the Phase I effort we became aware of a publication detailing some of the crucial parameters of the Cr^{3+}-Er^{3+} interaction in large-lattice garnets[7] and articles were published by the group describing some of their efforts on study of the Cr^{3+}-Ho^{3+} and Cr^{3+}-Tm^{3+} interactions.[8,9] In addition, Shcherbakov presented an invited paper at the CLEO '86 Conference in San Francisco[10], and a seminar at the Massachusetts Institute of Technology (June, 1986) describing results of laser experiments on two systems, Er,Cr:$Y_3Sc_2Ga_3O_{12}$ (YSGG) at 2800 nm and Ho,Tm,Cr:YSGG at 2100 nm. The reported performance of the systems showed a significant improvement over existing Er and Ho lasers. When we began our Phase I program, we changed the host crystal to be studied from GSGG to YSGG, based on the Soviet data. YSGG appears to have the strongest Cr^{3+}-Er^{3+} interaction[7] and may be better suited than GSGG in accepting the high Er^{3+} doping levels needed for efficient Cr^{3+}-Er^{3+} transfer.

In the Sections below we describe the results of our Phase I research effort on the Er,Cr,YSGG system. In summary, we contracted to have a crystal of Er,Cr:YSGG grown at Airtron Solid State and Materials Group (Morris Plains, New Jersey), carried out a series of spectroscopic measurements on the material grown and obtained the first laser action from Er,Cr:YSGG outside of the Soviet Union. Our laser data, confined to study of the $^4I_{11/2} \rightarrow ^4I_{13/2}$ laser transition, confirmed that the system performance was substantially superior to established 2700-2900 nm Er^{3+} lasers, such as Er:YAG and Er:YLF, and our results improved on the announced Soviet data.

2 Crystal Growth

The growth of a crystal of Er,Cr:YSGG was carried out at Airtron under the supervision of Robert Uhrin. We specified doping levels for the material of 4.7×10^{21} cm⁻³ and 2×10^{20} cm⁻³ of Er^{3+} and Cr^{3+} ions, respectively, based on Soviet data[10] on systems optimized for laser operation on the $^4I_{11/2} \rightarrow ^4I_{13/2}$ transition in the 2800-nm wavelength region. The doping level for Er^{3+} results in approximately 1/3 of the Y^{3+} ions being replaced by Er^{3+} ions. In preparing the initial charge for the melt, oxide powders of the general composition M_2O_3 were used, where M is one of the metallic ions. Weight percentages for the oxide powders were 27.03, 22.89, 16.51, 33.21 and 0.36 for Y, Er, Sc, Ga, and Cr oxides, respectively, with the weight percentages calculated on the basis of distribution coefficients for Er and Cr of 1.1 and 1.0, respectively. The standard Czochcralski technique for growth of oxide garnets was used, involving an rf-heated iridium crucible maintained in a slighly oxygen-rich atmosphere. The boule grown represented 18.2% of the total melt, was approximately 30-mm in diameter and 100-mm in length and was free of cracks. Sections from both ends of the boule were cut off and polished for spectroscopic measurements and one laser rod, 6.3-mm in diameter and 76-mm in length was extracted by core drilling in the bulk of the boule. The region for coring was determined by visually examining the length of the boule through crossed polarizers to search for minimal stress-induced birefringence. Examination was made difficult by the strong optical absorption in the material. Optical absorption measurements, described in the following Section, showed that there was only a slight variation in the concentration of either dopant along the length of the boule, confirming the assumption of near-unity segregation coefficients for both Er and Cr in YSGG.

3 Spectroscopic Data and Analysis

3.1 Absorption Data

Absorption measurements in general were carried out with the use of a Perkin-Elmer Lambda 9 dual-beam spectrophotometer. A digitized version of the spectrophotometer output was fed via an RS-232 serial connection to a microcomputer for analysis and plotting. The absorption coefficients for the Er^{3+} transitions had peak values of tens of inverse centimeters and thus thin samples had to be used to keep the spectrophotometer measurements within range. The data presented below was taken with a 0.173-cm thick sample unless noted. In the Figures the Fresnel loss from the sample surfaces has not been subtracted.

Figure 1 shows a relatively low-spectral-resolution scan of the thin-sample absorption over the range 300-750 nm, showing the narrow-line Er^{3+} transitions superimposed over the two broad Cr^{3+} absorption bands, $^4A_2 \rightarrow {}^4T_2$ peaking at 640 nm and $^4A_2 \rightarrow {}^4T_1$ peaking at 450 nm. The assignments shown for the Er^{3+} transitions denote the upper level of the transition (the lower level is the $^4I_{15/2}$ state) and are based on the energy-level ordering shown in the Diecke diagram for Er^{3+}.

The remaining absorption data presented shows details for each of the Er^{3+} transitions. Figure 2 is absorption to the $^4I_{13/2}$ state and shows three groups of transitions; two groups of narrow, intense lines from 1450-1500 nm and 1500-1550 nm and a group of weaker, broad lines from 1550-1650 nm. The latter, "hot bands", originate from higher lying states of the $^4I_{15/2}$ manifold and are lifetime broadened. The group from 1450-1500 nm are transitions from the lowest ground-state levels to a cluster of high-energy levels of the $^4I_{13/2}$ state while the 1500-1550-nm group terminate on the lowest-energy levels of that state. In Fig. 3 we show the weak hot bands in more detail. The data is actually two curves, one from a 0.772-cm-thick sample cut from the top, or first-to-freeze end of the Er,Cr:YSGG boule and the other from a 0.663-cm sample cut from the boule bottom end. The near-perfect overlap of the curves indicates that there was essentially no concentration gradient for Er^{3+} ions along the length of the boule and that the distribution coefficient for Er in YSGG must be close to unity.

The next set of four Figures are similar to Figs. 2 and 3 in that they show both the full absorption-band data, derived from the thin sample, and hot-band details derived from a thicker sample, in this case the 0.772-cm-thick crystal. Figures 4 and 5 are for the $^4I_{11/2}$ state while Figs. 6 and 7 are for the $^4I_{9/2}$ state. The last set of Figures (8-11) for absorption data cover details of the Er^{3+} absorption over the wavelength region 300-700 nm, superimposed on a background of Cr^{3+} absorption.

We did not attempt to determine all of the energy levels of the Er^{3+} ion from the absorption data above, but concentrated our efforts on the levels from the ground state $^4I_{15/2}$ to the $^4I_{9/2}$ excited state. The number of possible transitions for a given absorption band can be large. For example, the ground-state to first-excited-state ($^4I_{13/2}$) absorption consists of a possible 56 transitions, given lower- and upper-level degeneracies of 8 and 7, respectively. Such a large number makes analysis of the absorption data difficult. In order to help sort out the transitions we also measured absorption in the thin sample cooled to 77K. The lines narrowed to such an extent that the peak absorption for many of the strongest lines was greater than the upper limit of measurement for the spectrophotometer, even for the thin sample. For this reason we do not reproduce the low-temperature in this report. With narrower absorption lines and the elimination of hot bands the spectra were easier to interpret. Table 1 lists the manifold energy levels for the various states. Also included is published data[11] on the energy levels of Er:YAG and Er:Lu$_3$Al$_5$O$_{12}$(LuAG). We note a general trend in the YSGG host is to smaller manifold splittings compared to the two other garnet crystals, which is reasonable given the smaller crystal fields expected in the larger YSGG lattice.
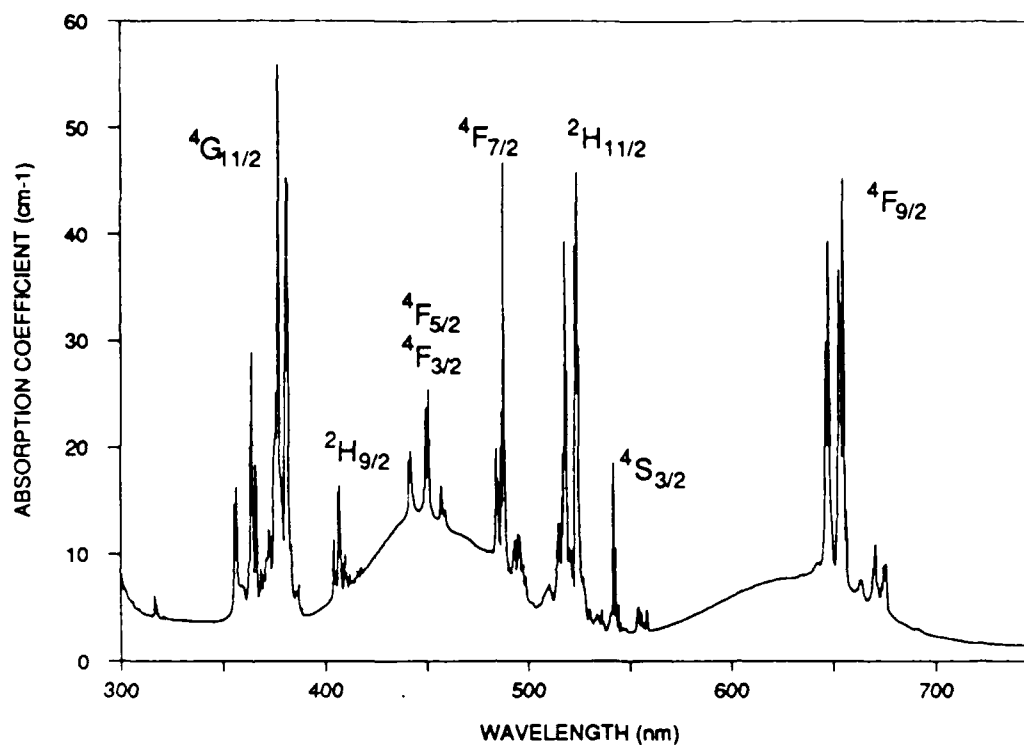
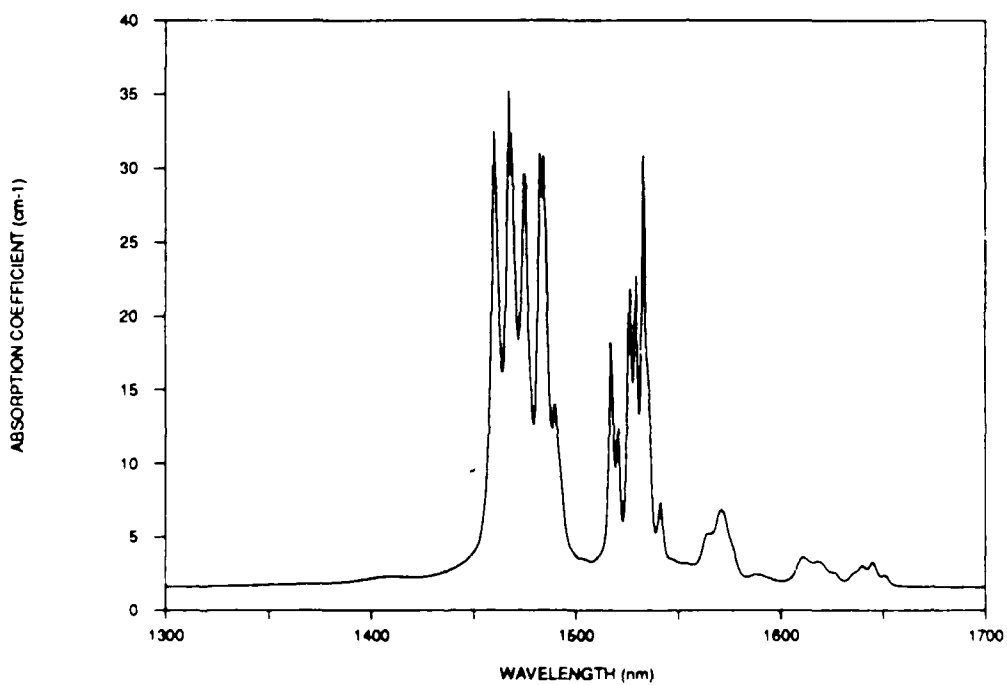Figure 1. Low-resolution absorption spectrum of Er,Cr:YSGG.

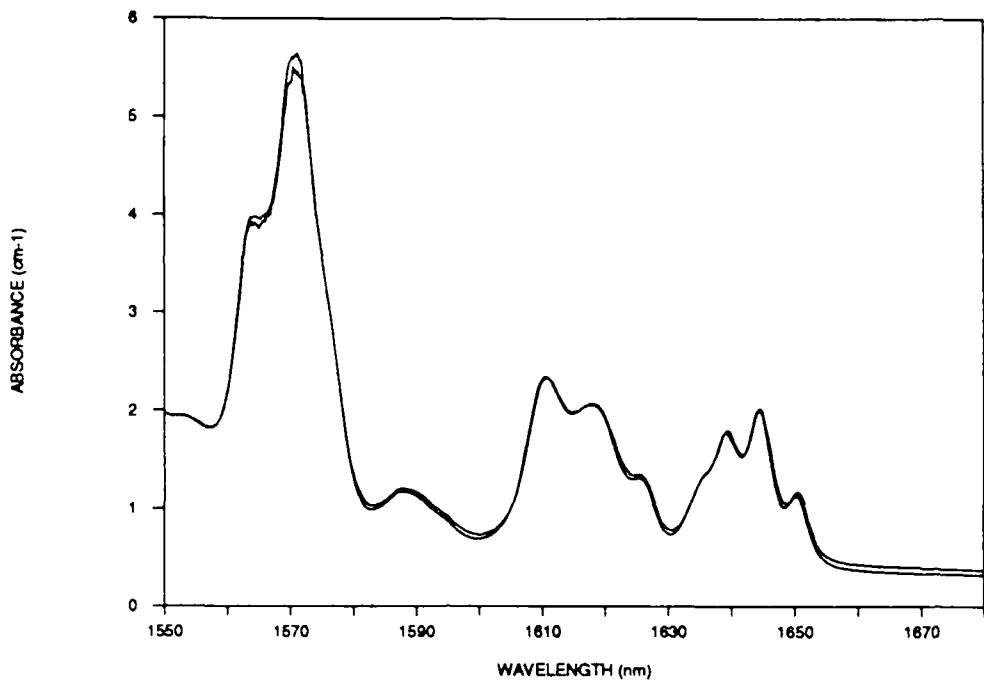

Figure 2. $^4I_{13/2}$ absorption band of Er^{3+}.

Figure 3. $^4I_{13/2}$ hot-band absorption for samples from top and bottom of boule.
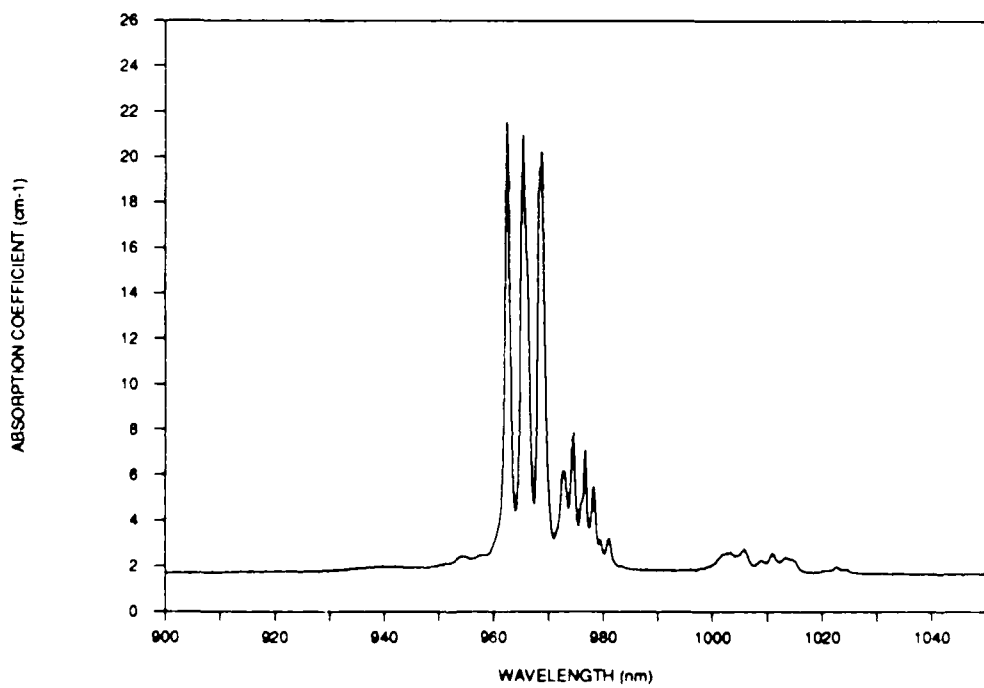

Figure 4. $^4I_{11/2}$ absorption band of Er^{3+}.
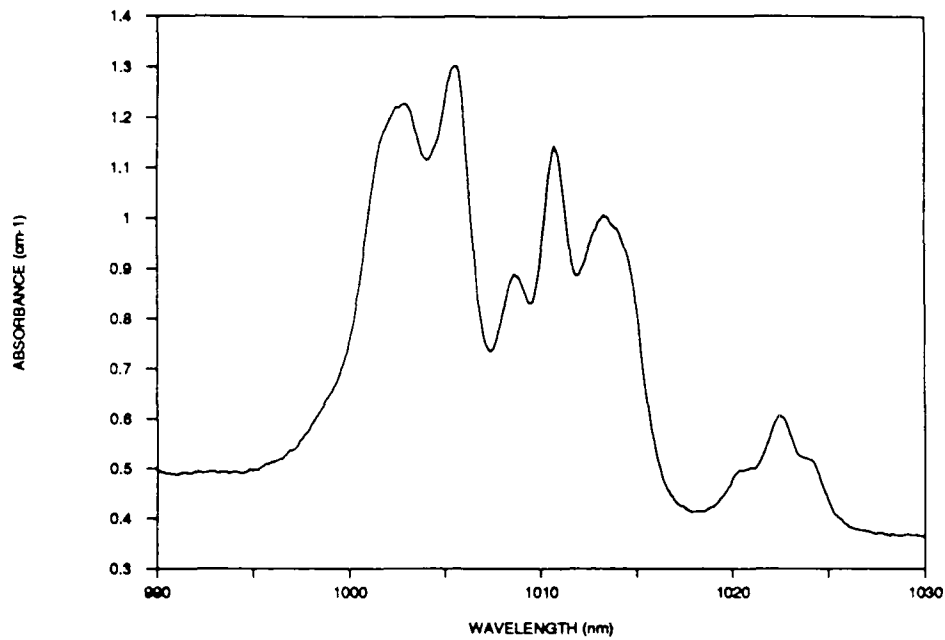
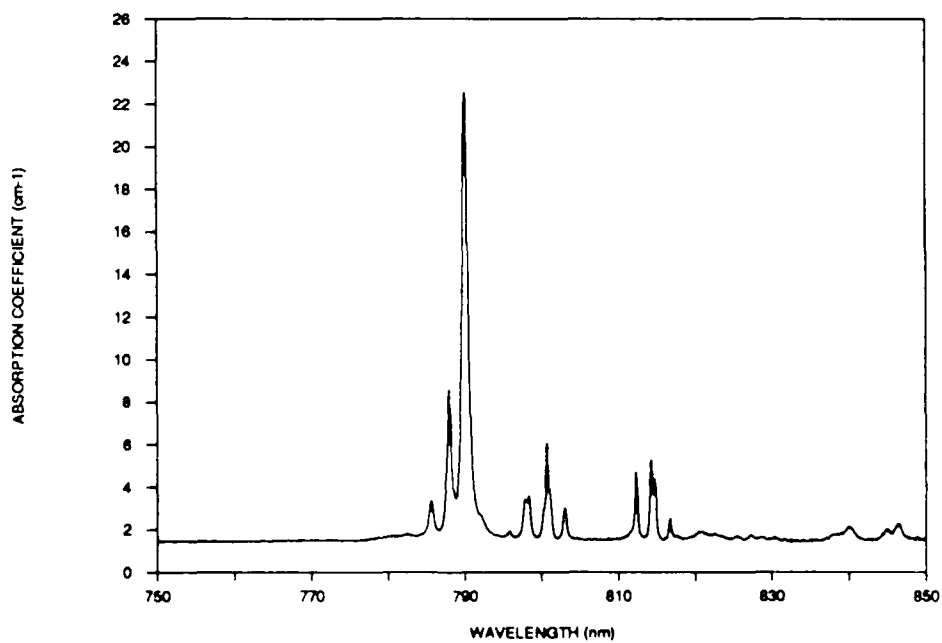Figure 5. $^4I_{11/2}$ hot-band absorption of Er^{3+}.

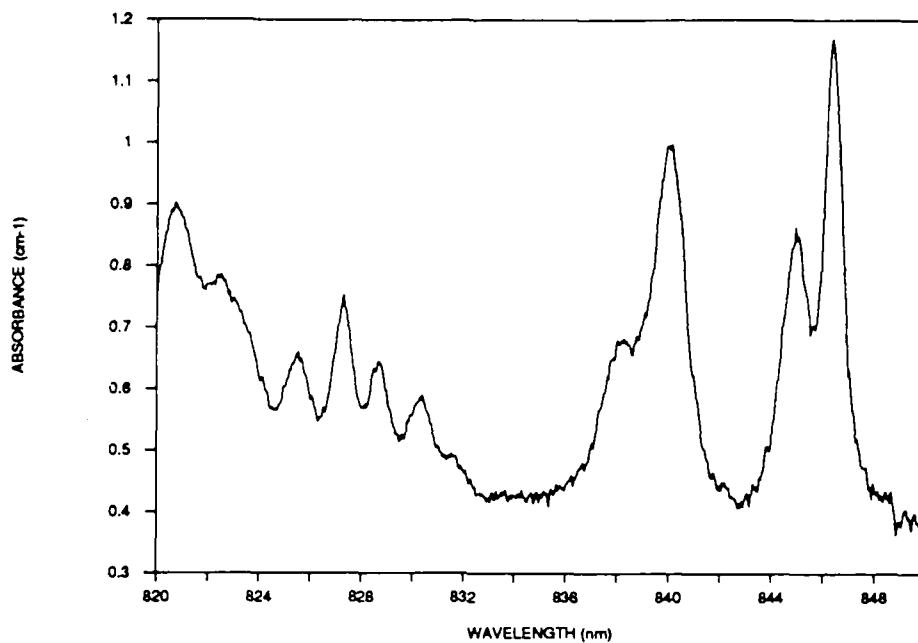Figure 6. $^4I_{9/2}$ absorption band of Er^{3+}.

Figure 7. $^4I_{9/2}$ hot-band absorption of Er^{3+}.
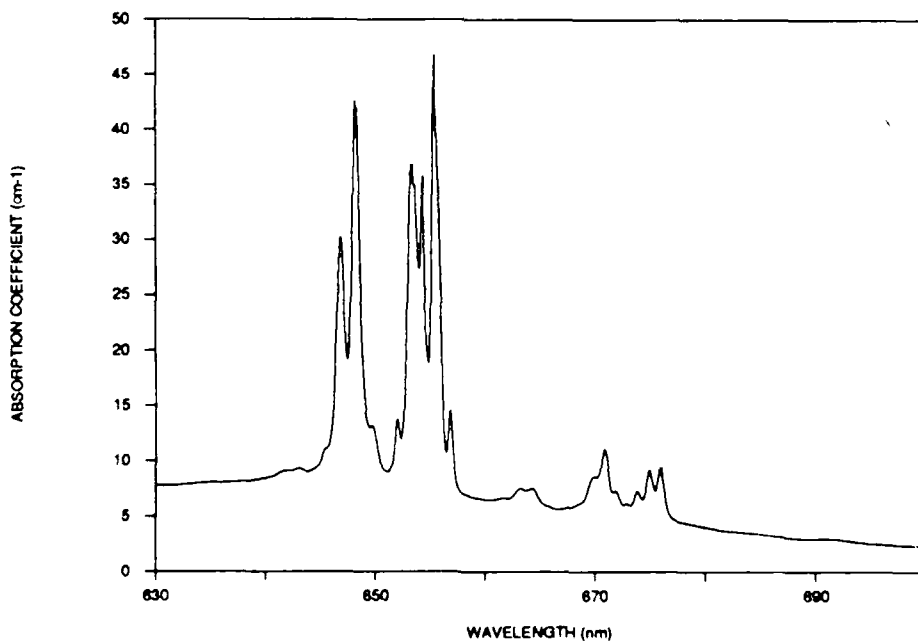

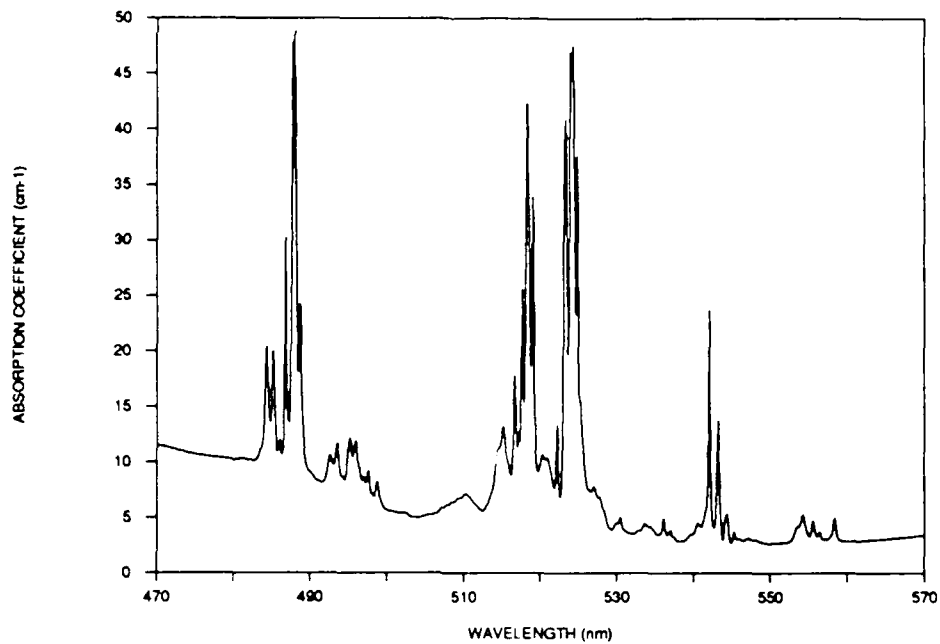Figure 8. Absorption from 630-700 nm.
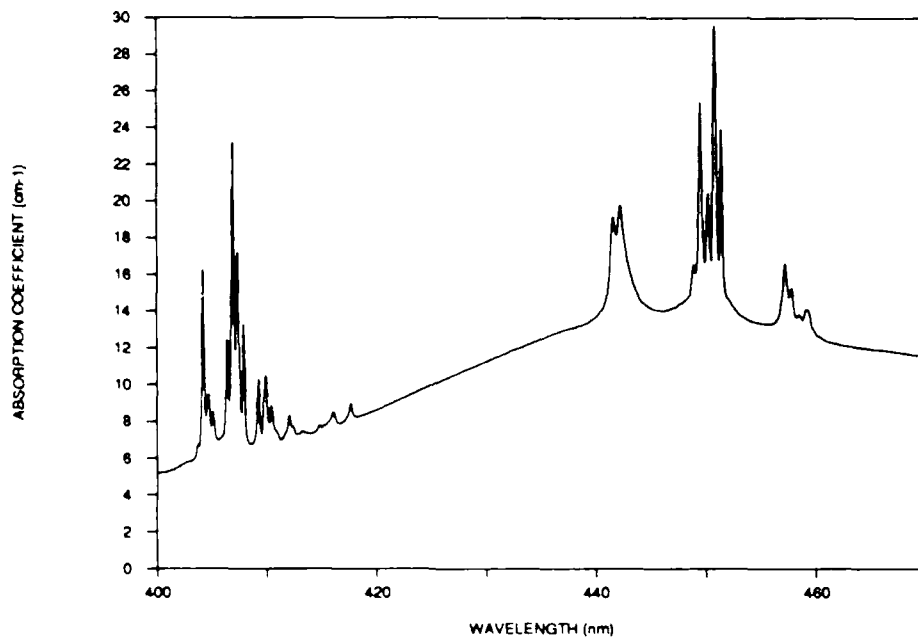
Figure 9. Absorption from 470-570 nm.

Figure 10. Absorption from 400-470 nm.

8

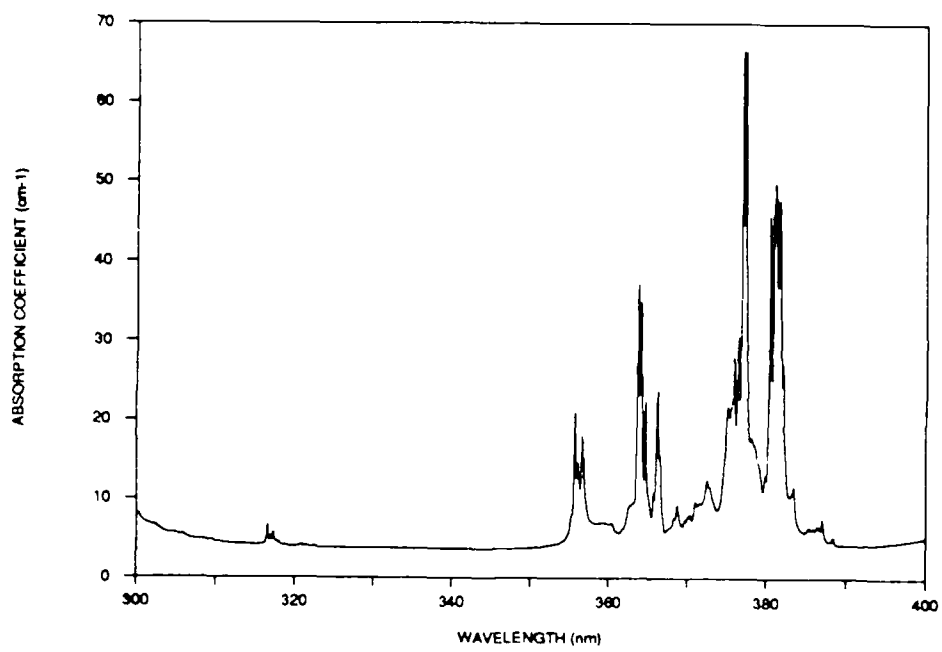Figure 11. Absorption from 300-400 nm.

Table 1. Energy levels (cm⁻¹) of Er³⁺ in different host crystals

State	Er,Cr:YSGG	Er:YAG	Er:LuAG
$^4I_{9/2}$	12742	12760	12772
	12698	12713	12731
	12574	12572	12580
	12527	12524	12532
	12312	12301	12300
$^4I_{11/2}$	10400	10412	10420
	10397	10408	10415
	10360	10367	10381
	10352	10356	10370
	10285	10285	10285
	10269	10252	10264
$^4I_{13/2}$	6848	6879	6885
	6786	6818	6847
	6726	6800	6818
	6706	6779	6798
	6597	6602	6602
	6581	6596	6595
	6566	6544	6559
$^4I_{15/2}$	496	568	578
	476	523	534
	405	424	450
	380	411	434
	72	76	76
	41	57	53
	35	19	32
	0	0	0

3.2 Fluorescence Spectra

Fluorescence spectra were taken for two Er³⁺ transitions, the $^4I_{13/2} \rightarrow ^4I_{15/2}$ emission in the 1600-nm wavelength region and the $^4I_{11/2} \rightarrow ^4I_{13/2}$ emission around 2800 nm. Samples were excited by a cw argon-ion laser, the output of which was mechanically chopped to allow synchronous detection by a lock-in amplifier. An ISA HR-640, 0.68-m grating spectrometer, with a 300 g/mm grating, was used to disperse the sample emission, and a PbS photoconductive cell, cooled by dry ice, was used for detection. A microcomputer with a custom software routine controlled, over RS-232 channels, both the stepper-motor drive to the grating and the lock-in amplifier. The digital output of the lock-in amplifier was recorded directly to a floppy-disk file by the control program. The spectral response of the system in both wavelength regions was calibrated by use of a tungsten standard lamp (DXY-1000) placed at the sample location. All the data shown below is corrected for the system response. The inside of the the spectrometer was purged with dry nitrogen for the measurement of 2800-nm emission in order to reduce the effects of atmospheric water vapor absorption on the spectral measurements.

The spectra for Cr³⁺ emission in the 750-nm wavelength region was observed under similar conditions, except that a GaAs-surface photomultiplier tube was used as the detector and the spectrometer was setup with a 1200-g/mm grating. As for the other emission data, the system response was corrected by use of data obtained with a tungsten standard lamp.

3.2.1 1600-nm emission

In Fig. 12 we show the emission spectrum from $^4I_{13/2} \rightarrow ^4I_{15/2}$ transitions, which appear over the range 1450-1650 nm. There was considerable self-absorption of emission in the sample examined because of the large absorption coefficients (see Fig. 2) associated with the high Er³⁺ doping level. The region below 1550 nm was particularly affected by self absorption. Thus the spectrum shown does not accurately reflect the relative intensities of the different transitions.
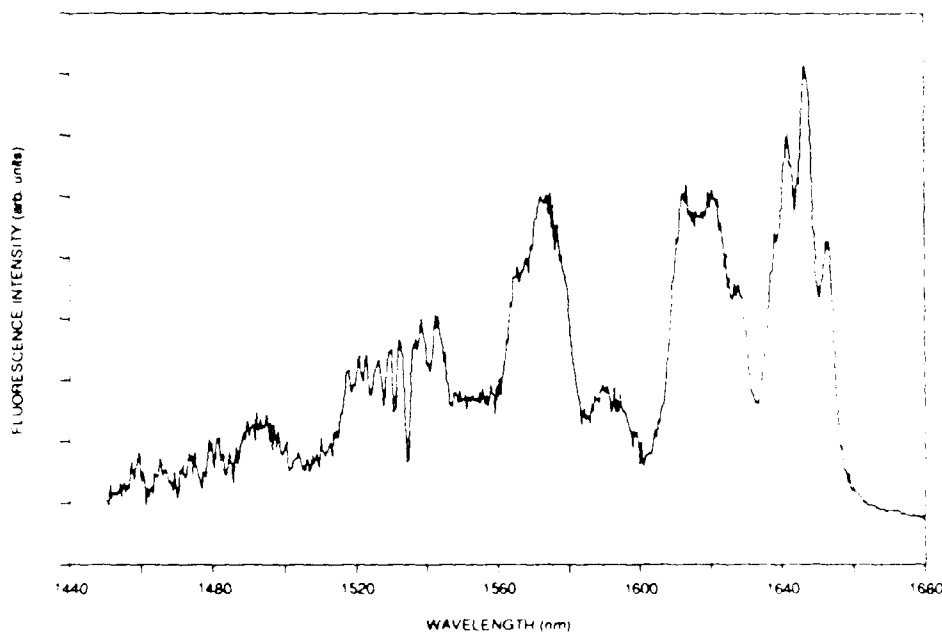

Figure 12. Emission spectrum from $^4I_{13/2} \rightarrow ^4I_{15/2}$ transitions.

11

The lowest-threshold laser operation from the transitions would occur for those terminating on the upper levels of the $^4I_{15/2}$ manifold, i.e. the same transitions associated with the hot-band absorption detailed in Fig. 3. In Fig. 13 we show in more detail the emission spectrum associated with high-lying levels of the $^4I_{15/2}$ state; the spectrum can be compared directly with Fig. 3.
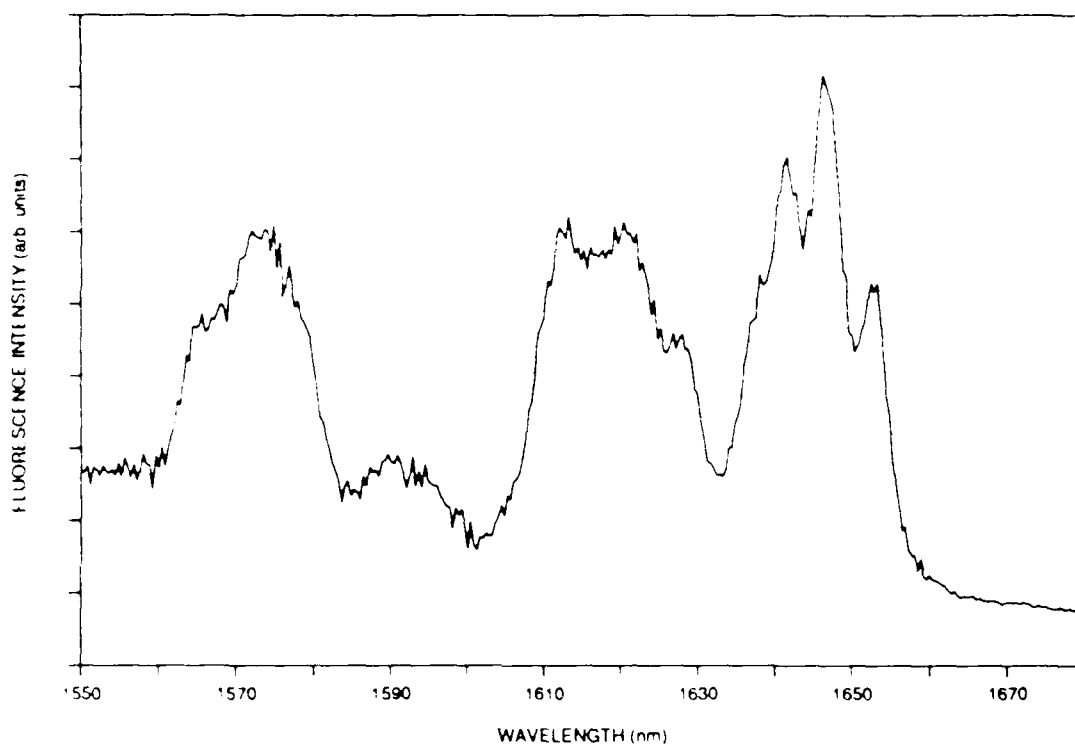

Figure 13. Emission spectrum to high-lying $^4I_{15/2}$ levels.

We have calculated the wavelengths of all possible transitions among the 4 highest-lying levels of the $^4I_{15/2}$ manifold and all the levels of the $^4I_{13/2}$ state, and these are tabulated in Table 2, ordered by increasing wavelength. The numbering system for levels in each manifold, based on increasing energy, starts with 1 for the lowest energy state. Calculation of the oscillator strengths for each possible transition is beyond the scope of this study, and thus the table is only a start at understanding the data in Figs. 3 and 13. Many of the peaks appearing in the data are in fact the sum of several possible transitions, and thus the locations of the peaks may not correspond exactly to the calculated transition wavelengths. Laser operation at room temperature can most likely be obtained from the transitions in the wavelength region from 1634-1650 nm, since they originate on the low-lying states in the $^4I_{13/2}$ manifold, terminate on the two highest states of the $^4I_{15/2}$ manifold, and appear with high intensity in the fluorescence spectrum.

Table 2. Identification of possible $^4I_{13/2} \leftrightarrow {}^4I_{15/2}$ transitions.

Wavelength (nm)	Upper Level	Lower Level
1541	7	5
1552	7	6
1561	6	5
1567	6	6
1569	7	7
1575	7	8
1576	5	5
1581	4	5
1582	5	6
1585	6	7
1587	4	6
1591	6	8
1600	5	7
1605	4	7
1606	5	8
1608	3	5
1611	4	8
1613	2	5
1615	3	6
1617	1	5
1619	2	6
1623	1	6
1634	3	7
1638	2	7
1640	3	8
1642	1	7
1644	2	8
1649	1	8

13

3.2.2 2800-nm Emission

The terminal level for the 2800-nm-region $^4I_{11/2} \rightarrow {}^4I_{13/2}$ emission is high enough in energy to eliminate any problems with self-absorption. Thus our data is an accurate indication of the relative line strengths of all the different transitions. Figure 14 presents the spectrum over the full range of observed emission, 2500-3000 nm. It should be noted that the calibration curve for the tungsten lamp standard does not extend beyond 2500 nm. We assumed that the lamp spectral response was well approximated by a 3000-K blackbody in performing the system response correction to the measured Er^{3+} emission.
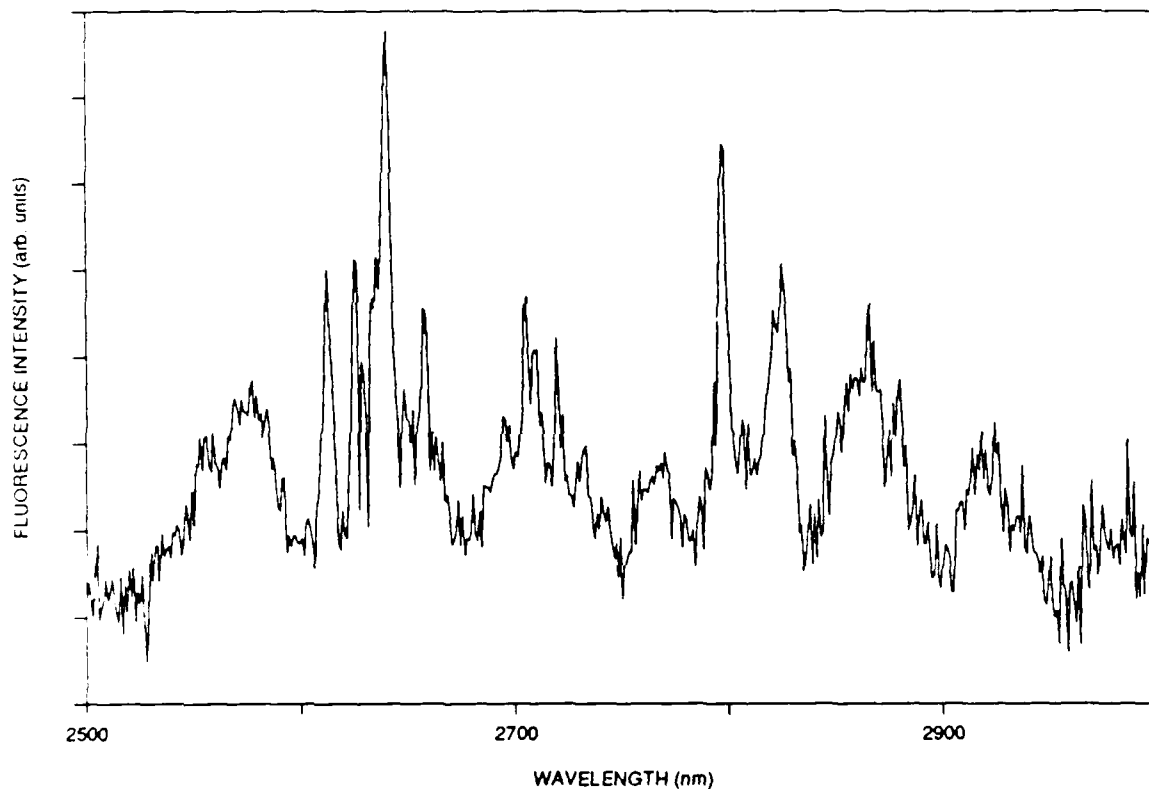

Figure 14. Emission spectrum from $^4I_{11/2} \rightarrow {}^4I_{13/2}$ transitions.

We have calculated the wavelengths of all possible transitions, based on the Er^{3+} energy levels in Table 1, and present the results of our calculations in Table 3. The labelling of upper and lower levels is in the same format used in Table 2. In addition, we have plotted in Figs. 15 and 16 the data of Fig. 14 with the addition of markers indicating the positions of the various transitions. Each set of markers is associated with a different upper level, with Fig. 15 covering the 4 lowest-energy states and Fig. 16 covering the two highest levels in the $^4I_{11/2}$ manifold. It is evident that most of the lines in the observed spectrum can be accounted for. However, the broad peaks centered at 2577 and 2975 nm cannot be identified with any transition and may be associated with pairs of Er^{3+} ions or unidentified impurities in the crystal.

14

Table 3. Identification of possible $^4I_{11/2} \rightarrow {}^4I_{13/2}$ transitions.

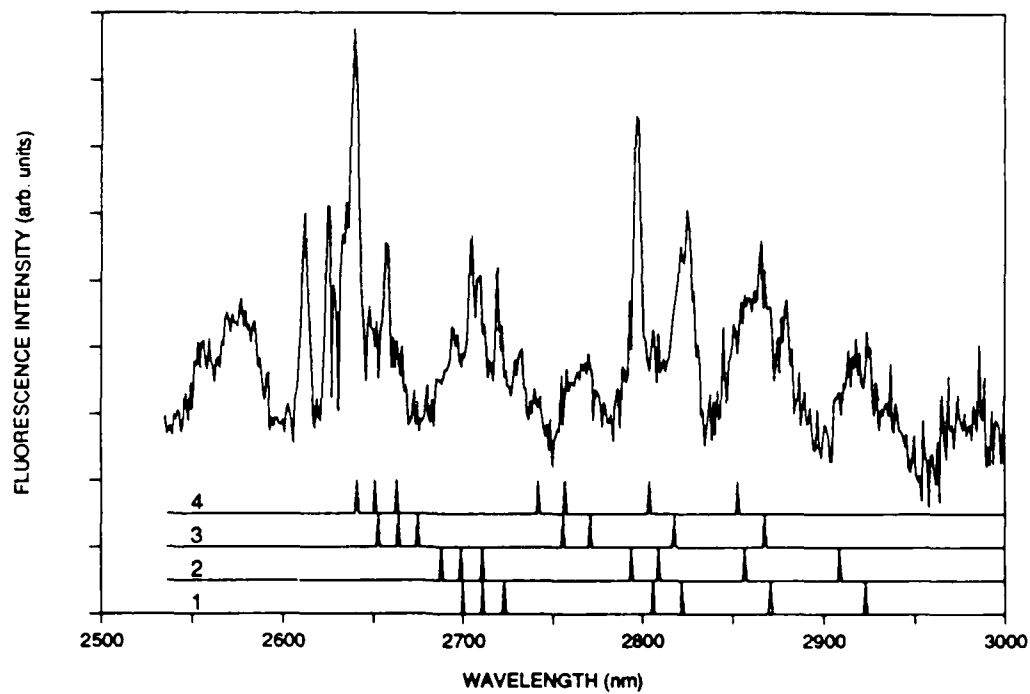| Wavelength (nm)	Upper Level	Lower Level
2608	6	1
2610	5	1
2618	6	2
2620	5	2
2629	6	3
2631	5	3
2641	4	1
2651	4	2
2653	3	1
2663	4	3
2664	3	2
2675	3	3
2688	2	1
2699	2	2
2700	1	1
2707	6	4
2709	5	4
2711	2	3
2711	1	2
2721	6	5
2723	1	3
2724	5	5
2742	4	4
2756	3	4
2757	4	5
2767	6	6
2769	5	6
2771	3	5
2794	2	4
2804	4	6
2806	1	4
2809	2	5
2815	6	7
2817	5	7
2818	3	6
2822	1	5
2853	4	7
2857	2	6
2868	3	7
2871	1	6
2909	2	7
2923	1	7

Figure 15. Line positions of transitions from 4 lowest-energy levels of $^4I_{11/2}$ state.
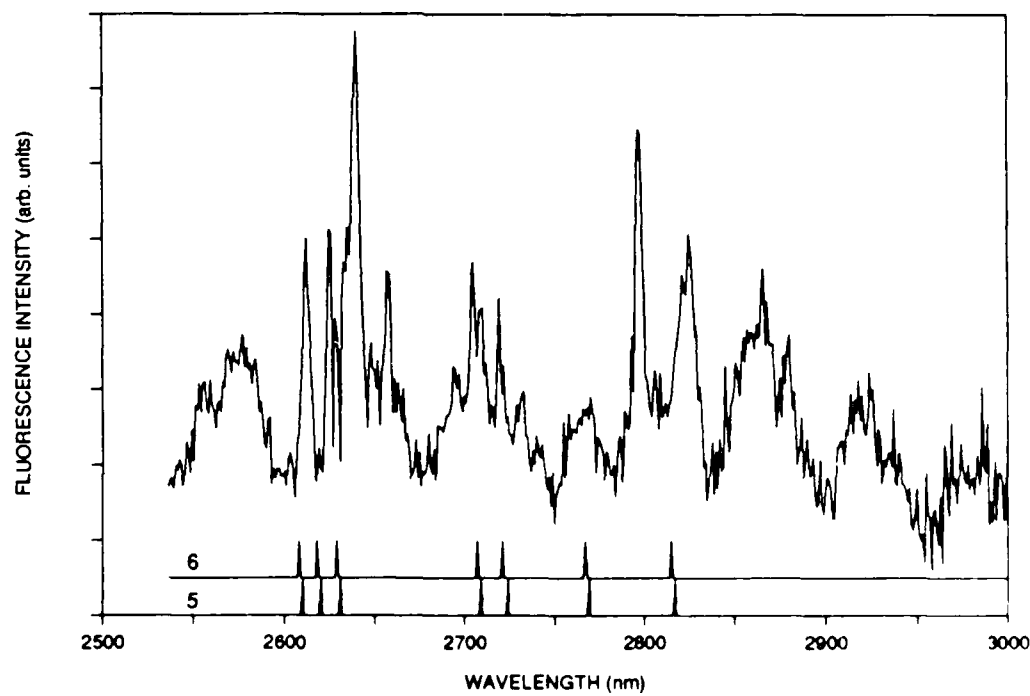

Figure 16. Line positions of transitions from 2 highest-energy levels of $^4I_{11/2}$ state.

16

3.2.3 Cr^{3+} Emission

In general the emission from the $^4T_2 \rightarrow {}^4A_2$ band of Cr^{3+} was weak, and could only be observed by the use of a photomultiplier tube in the detection system. Careful choice of the excitation wavelength was necessary to avoid interference from Er^{3+} fluorescence in the visible and near-infrared. Fig. 17 shows the broadband emission from Cr^{3+}, peaking at 740 nm, obtained with an excitation wavelength of 476.5 nm. Examination of Figs. 1 and 9 shows that this wavelength falls well outside any Er^{3+} absorption bands, while being near the peak of the $^4A_2 \rightarrow$ $^4T_1$ absorption band of Cr^{3+}. Line emission from Er^{3+} transitions in the 840-860-nm region is still evident, however. Based on previous data for Er^{3+} in other garnets[11] we conclude that the Er^{3+} fluorescence is from $^4S_{3/2} \rightarrow {}^4I_{13/2}$ transitions. It is possible that the Er^{3+} ions are excited to the $^4S_{3/2}$ level by direct absorption in the wings of the Er^{3+} absorption lines near 476.5 nm, but it may be that Er^{3+} ions are excited to the $^4S_{3/2}$ state by the well-known process of cross-relaxation[12] between pairs of excited Er^{3+} states. The initial excitation of single Er^{3+} ions would proceed via the Cr^{3+}-Er^{3+} nonradiative transfer process, and cross relaxation would then promote one Er^{3+} ion to the higher-energy $^4S_{3/2}$ state.

The dip in observed emission intensity around 790 nm is due absorption in the crystal by the $^4I_{9/2}$ Er^{3+} band. The good spectral overlap between Cr^{3+} emission and Er^{3+} absorption is one of the factors leading to efficient nonradiative transfer from Cr^{3+} to Er^{3+}.
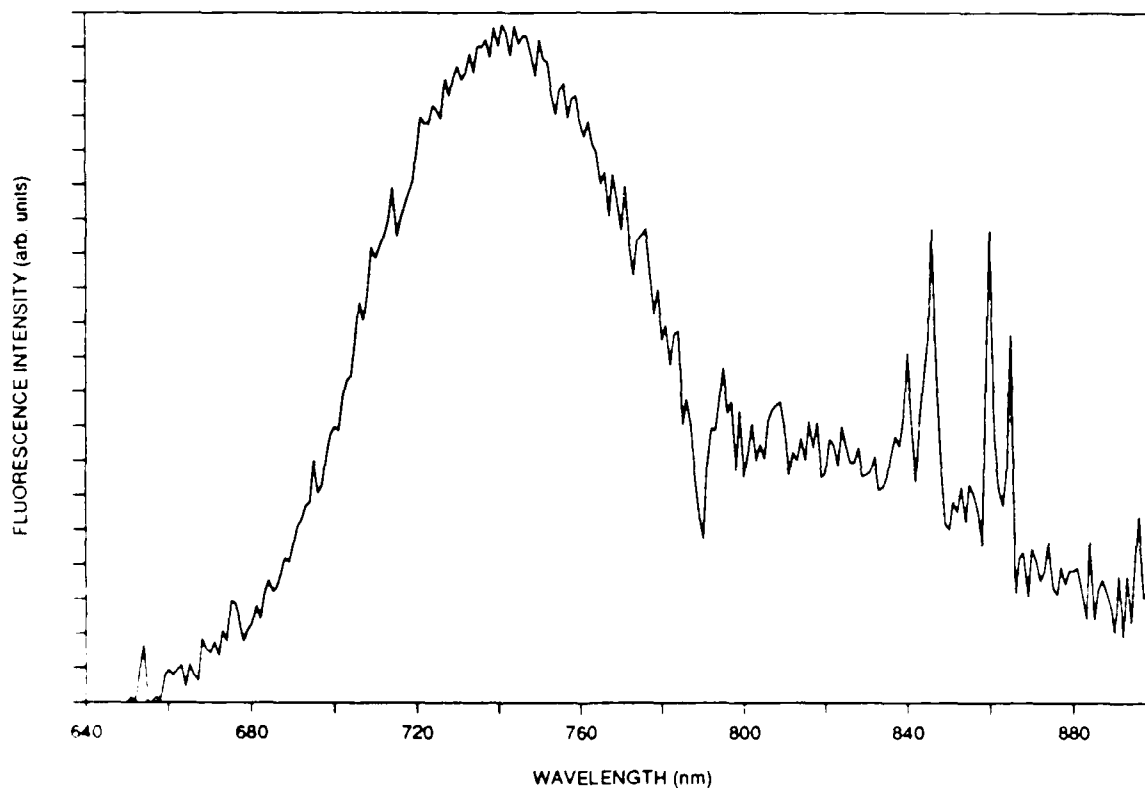

Figure 17. Emission from Er,Cr:YSGG with 476.5-nm excitation.

17

In Fig. 18 we show the measured emission in the same wavelength region as that of the previous figure, but taken with an excitation wavelength of 514.5 nm, which coincides with a region of strong Er^{3+} absorption (see Fig. 1) as well as absorption from Cr^{3+}. The lower trace in the figure shows the relative intensities of the Cr^{3+} emission and the peak Er^{3+} emission line at 860 nm. In the top trace the gain of the detection system was increased to show the low-level Cr^{3+} emission. It is interesting to note the presence of weak emission lines in the 790-830-nm region, which could be the result of $^4I_{9/2} \rightarrow {}^4I_{15/2}$ Er^{3+} transitions. The weak emission apparently overcomes the absorption-related dip in Cr^{3+} emission evident Fig. 16.

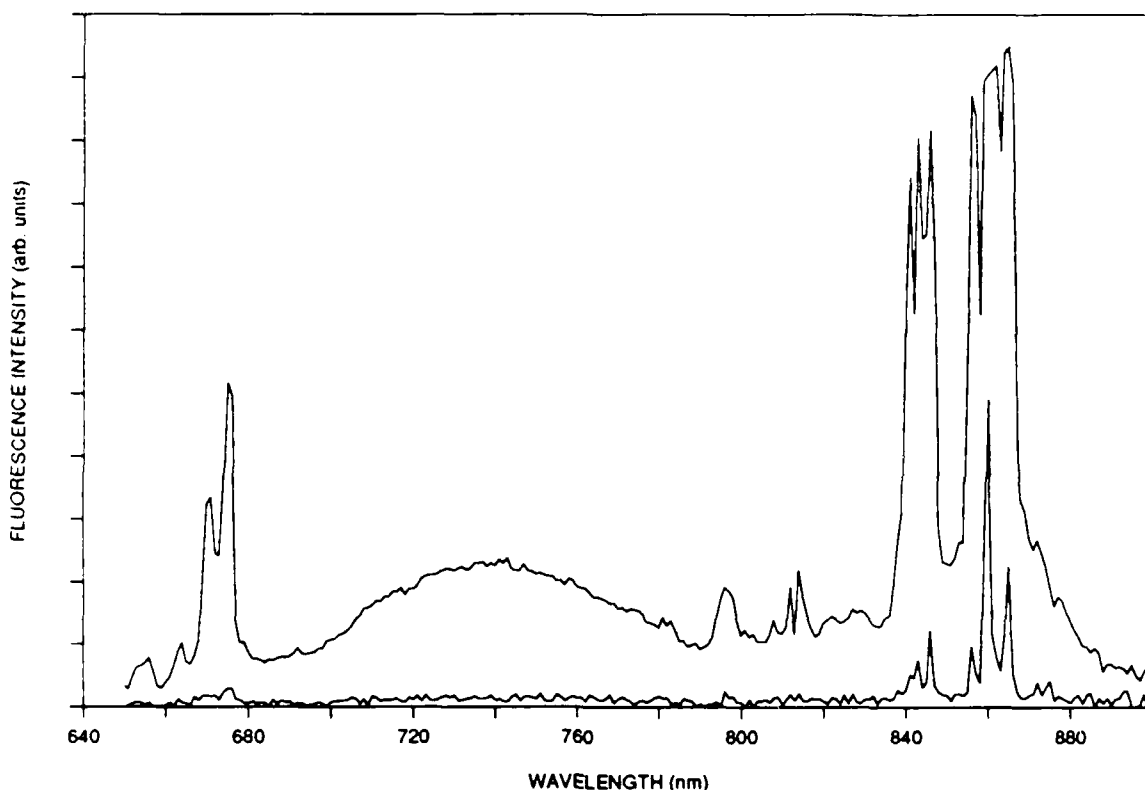Figure 18. Emission from Er,Cr:YSGG with 514.5-nm excitation.

We can conclude that the relative low intensity of Cr^{3+} emission in the Er,Cr:YSGG crystal is the result of the low quantum efficiency of the $^4T_2 \rightarrow {}^4A_2$ transition, which in   he result of nonradiative transfer to Er^{3+} ions. Our measurements of the Cr^{3+} fluorescenc   time, discussed below, also confirm this conclusion.

3.3 Excitation Spectra

The excitation spectra for Er^{3+} emission was measured by illuminating a 0.75-cm-thick Er,Cr:YSGG crystal with monochromatic light and observing the intensity of the fluorescence signal as a function of illumination wavelength. The monochromatic source, covering the wavelength range 250-850 nm, was provided by passing the output of a 75W xenon short-arc lamp through a 0.2-m grating spectrometer (ISA H-20) and had a spectral width of approximately 4 nm. The stepper-motor drive to the grating angle was controlled by the same computer hardware and software used for the fluorescence measurements described in Section 3.2. The

18

relative spectral intensity vs wavelength of the excitation system was determined by detection of the spectrometer output at the sample location with a pyroelectric detector-preamplifier, which had an essentially flat response over the entire excitation wavelength range. The excitation source was mechanically chopped and fluorescence was detected synchronously. As for the fluorescence-spectra measurements, the lock-in amplifier output was recorded directly to a computer disk file for later analysis. Fluorescence was observed at right angles to the excitation beam, filtered by appropriate elements and detected by a dry-ice-cooled PbS photoconductor.

Our interest in taking the data on excitation spectra was in determining the relative quantum efficiency of excitation as a function of wavelength, proportional to the fractional number of fluorescence photons per absorbed excitation photon. In the data shown below, the measured fluorescence signals as a function of excitation wavelength were divided by the measured relative excitation intensity as a function of wavelength, in order to provide properly normalized excitation spectra. Then, the intensity-corrected data was multiplied by the relative photon energy of the excitation source in order to determine the relative quantum efficiency.

3.3.1 2800-nm Emission

Emission in the 2800-nm wavelength region from the $^4I_{11/2} \rightarrow {}^4I_{13/2}$ transition was observed with a 2500-nm long-pass filter placed in front of the detector. Fig. 19 shows the emission intensity as a function of excitation wavelength, corrected as described above to show the relative quantum efficiency of excitation. The line structure in the 800-nm region is due to direct excitation into the Er^{3+} $^4I_{9/2}$ absorption band, while the broad band from 360-700 nm results from excitation into both the Cr^{3+} absorption bands and a variety of Er^{3+} transitions. The sample was thick enough to absorb essentially all of the excitation in this region, except for a small interval around 400 nm, hence the notable lack of structure. It is evident that excitation into the Cr^{3+} absorption bands is, within experimental error, as efficient as direct excitation into the Er^{3+} bands. The measurement does not indicate the absolute quantum efficiency of excitation of 2800-nm emission, but from the data we can conclude that the quantum efficiency is independent of the particular Cr^{3+} or Er^{3+} absorption transition over the range from 350-850 nm.
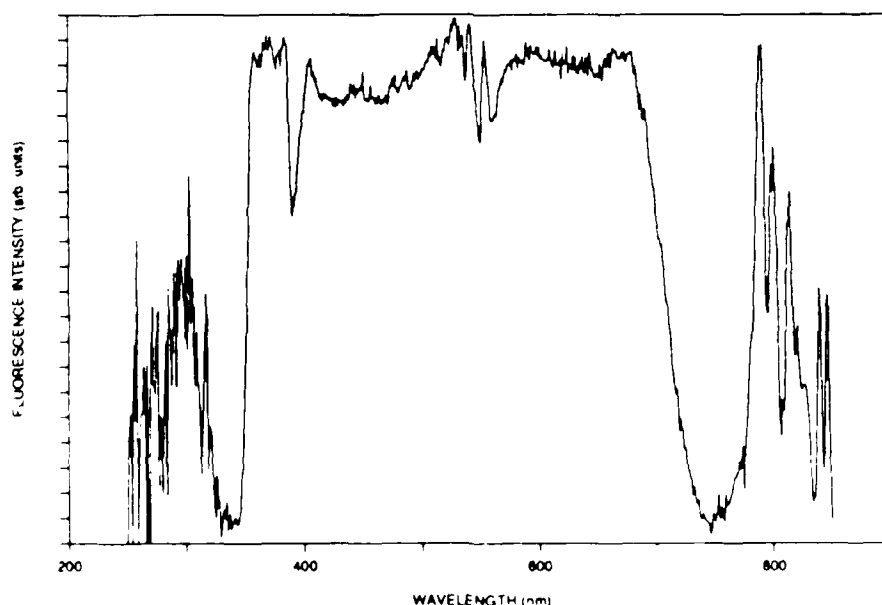

Figure 19. Excitation spectrum for $^4I_{11/2} \rightarrow {}^4I_{13/2}$ transitions at 2800 nm.

19

3.3.2 1600-nm Emission

A silicon window was placed in front of the detector to allow observation of the excitation spectrum for emission in the 1600-nm wavelength region from the $^4I_{13/2} \rightarrow {^4I_{15/2}}$ transition. A dielectric-coated mirror with high reflectivity from 2700-3000 nm was also placed in front of the detector to block fluorescence from the $^4I_{11/2} \rightarrow {^4I_{13/2}}$ transition. The excitation spectrum, shown in Fig. 20, is similar to that for 2800-nm emission, except that there appears to be an enhancement in excitation efficiency for Er^{3+} absorption transitions to the $^4S_{3/2}$ state (around 550 nm) and those at higher energies. As there are known emission bands from the $^4S_{3/2}$ state to lower levels, in particular 1200-nm and 1750-nm-wavelength transitions terminating on the $^4I_{9/2}$ and $^4I_{11/2}$ states, respectively, it is possible that the detection system also responded to emission from the $^4S_{3/2}$ level, distorting the excitation data for the $^4I_{13/2} \rightarrow {^4I_{15/2}}$ transition.
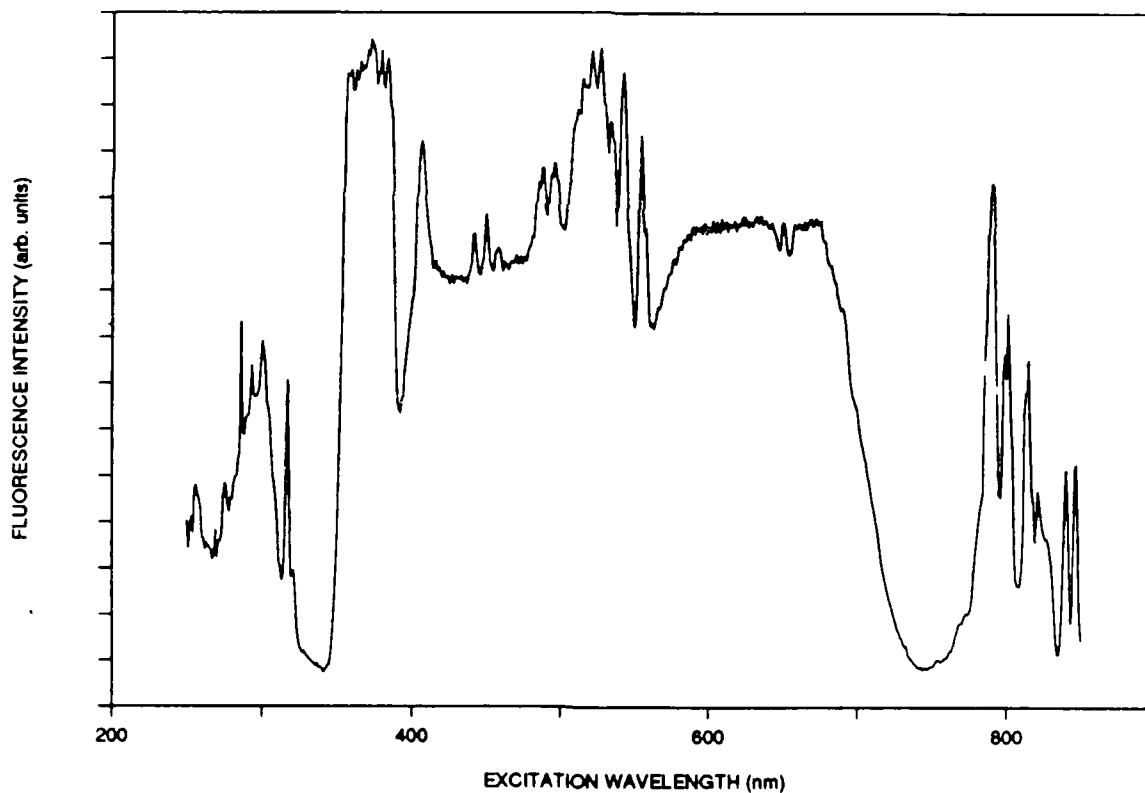

Figure 20. Excitation spectrum for $^4I_{13/2} \rightarrow {^4I_{15/2}}$ transitions at 1600 nm.

20

3.4 Fluorescence Buildup and Decay

We observed the time buildup and decay of fluorescence from Er,Cr:YSGG samples excited by two short-pulse laser systems. One laser was a nitrogen-laser-pumped dye laser (Laser Science VSL) used to excite Cr^{3+} ions and the other was a 790-nm $Ti:Al_2O_3$ laser (pumped by a q-switched, frequency-doubled Nd:YAG laser) used for direct excitation of Er^{3+} via the $^4I_{15/2} \rightarrow {}^4I_{9/2}$ transition. Fluorescence from Er^{3+} was observed by a liquid-nitrogen-cooled InSb photovoltaic detector, with a risetime of approximately 1 μsec, while Cr^{3+} fluorescence was detected by a photomultiplier tube. Appropriate dielectric filters were placed in front of the detectors to select the desired emission band. For the Cr^{3+} fluorescence we found it necessary to use a 10-nm-bandpass spike filter with a peak response at 750 nm in order to eliminate fluorescence from the $^4S_{3/2} \rightarrow {}^4I_{15/2}$ Er^{3+} transition around 850 nm. A Data Precision 6000 waveform analyzer recorded a digitized version of the decay signal, with the output of the analyzer fed to a microcomputer over a RS-232 serial channel.

3.4.1 2800-nm Buildup and Decay

Figure 21 shows the decay of 2800-nm emission excited at 790 nm. The logarithm of the decay signal is plotted, along with a straight line showing predicted decay for a single lifetime of 1.35 msec. The agreement between data and a single-lifetime model is good, and the deviation between observed and predicted signals at low signal levels may be the result of innacuracies in determining the signal baseline. Similar data appears in Fig. 22, for a dye-laser excitation source at 592 nm, which was absorbed by Cr^{3+} rather than Er^{3+} ions. The theoretical model for decay is based on a 1.4-msec lifetime.
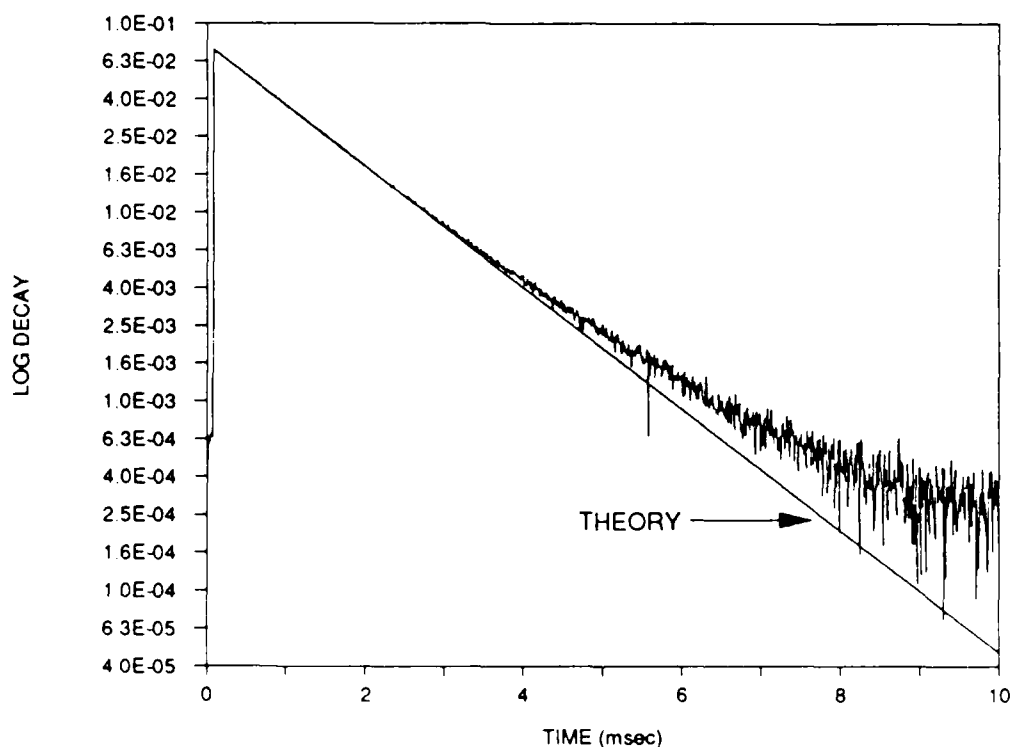

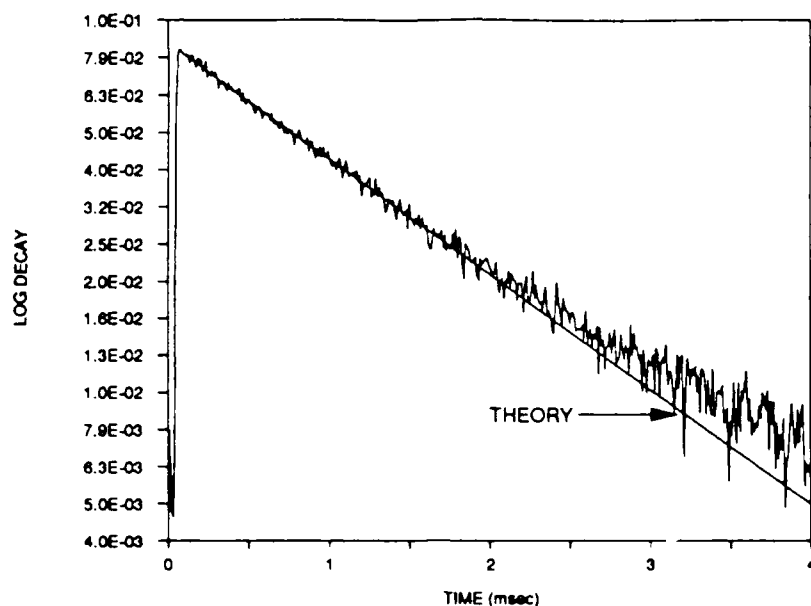Figure 21. Log decay for 2800-nm emission excited at 790 nm, with model.

Figure 22. Log decay for 2800-nm emission excited at 592 nm, with model.

The fact that there is essentially no difference between decay observed with direct and Cr^{3+}-transfer excitation indicates that the transfer rate from Cr^{3+} ions to Er^{3+} ions is fast compared to the Er^{3+} lifetime. This is confirmed by the data shown in Fig. 23, which shows the buildup of fluorescence for both 790- and 592-nm excitation. The two signals have been displaced from each other in time, for clarity. The buildup in both cases occurs in a microsecond, which is the approximate response time of the detector. From the buildup data we can conclude that both the Cr^{3+}-Er^{3+} transfer time and the the decay time of the $^4I_{9/2} \rightarrow {}^4I_{11/2}$ Er^{3+} transition are no greater than 1 microsecond.
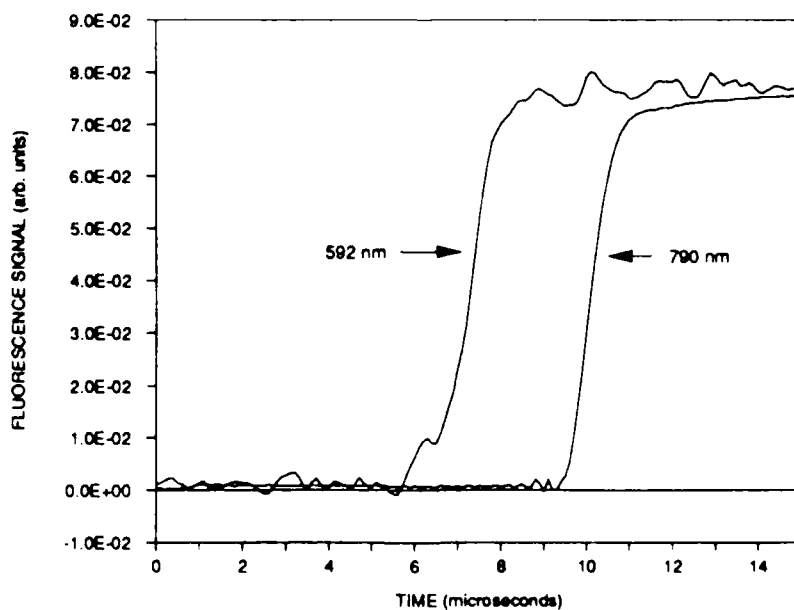

Figure 23. Buildup of 2800-nm emission for 592- and 790-nm excitation.

22

3.4.2   1600-nm Buildup and Decay

The only data taken for 1600-nm emission was for excitation by the 790-nm source, as we were unable to obtain an adequate signal-to-noise ratio for dye-laser excitation. Fig. 24 shows a portion of the observed signal, and indicates that the buildup time for 1600-nm fluorescence was considerably slower than for 2800-nm emission.
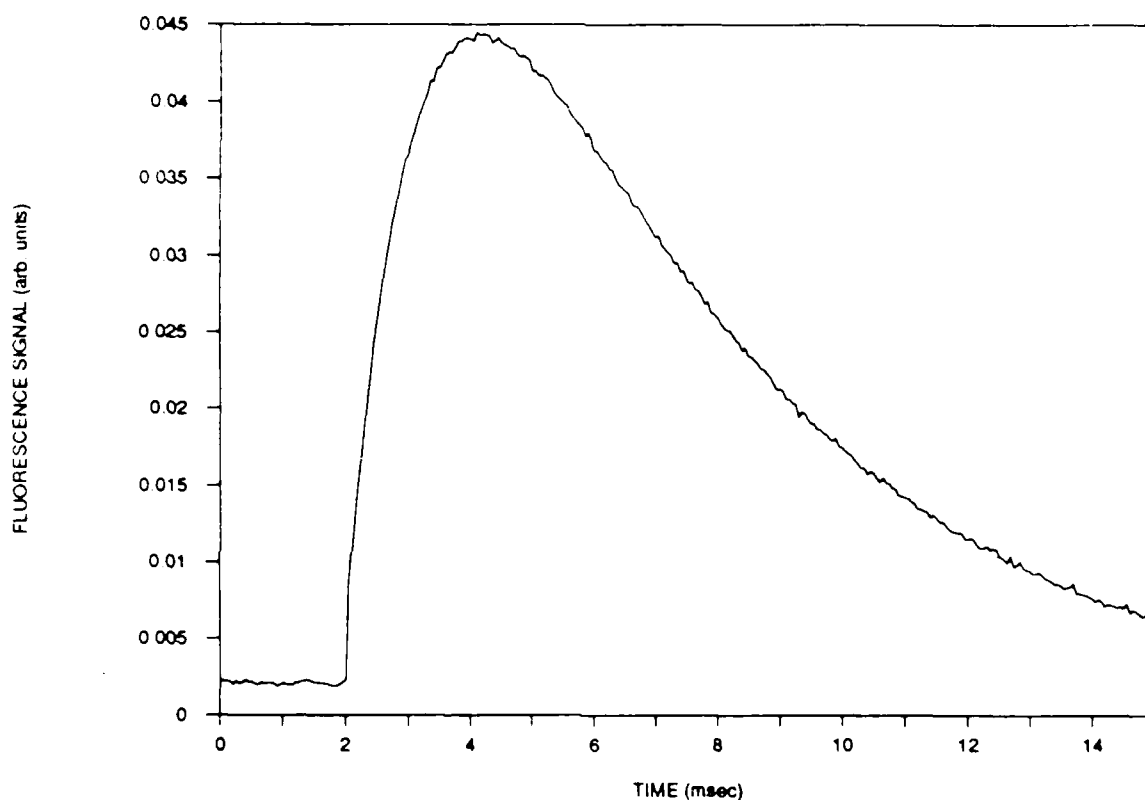

Figure 24. Response of 1600-nm emission to 790-nm short-pulse excitation.

We examined the 1600-nm buildup and determined that a single-rate buildup model provided a good fit to the data. Fig. 25 shows the observed fluorescence buildup signal and a model based on an exponential buildup with a 0.6-msec time constant. Since the 790-nm excitation source pumps the $^4I_{9/2}$ level, one would expect that, in the absence of any pair interactions between Er^{3+} ions, excitation transfer or excited-state absorption of the pump, the $^4I_{13/2}$ state (from which the 1600-nm emission originates) could be excited in only two ways. One is directly from the $^4I_{9/2}$ level and the other is from the $^4I_{11/2}$ level after that level is excited by a $^4I_{9/2} \rightarrow {}^4I_{11/2}$ transition. As noted above, the measurement of 2800-nm fluorescence buildup indicates that the $^4I_{9/2} \rightarrow {}^4I_{11/2}$ transition occurs in less than a microsecond, and thus excitation of the $^4I_{13/2}$ level directly from the $^4I_{9/2}$ level must be negligible. Since we measured a lifetime for the $^4I_{11/2} \rightarrow {}^4I_{9/2}$ transition of approximately 1.4 msec we would expect the same buildup time for 1600-nm fluorescence. The shorter observed buildup time indicates that the excitation process for 1600-nm emission is more complex than simple decay of levels in an isolated Er^{3+} ion.
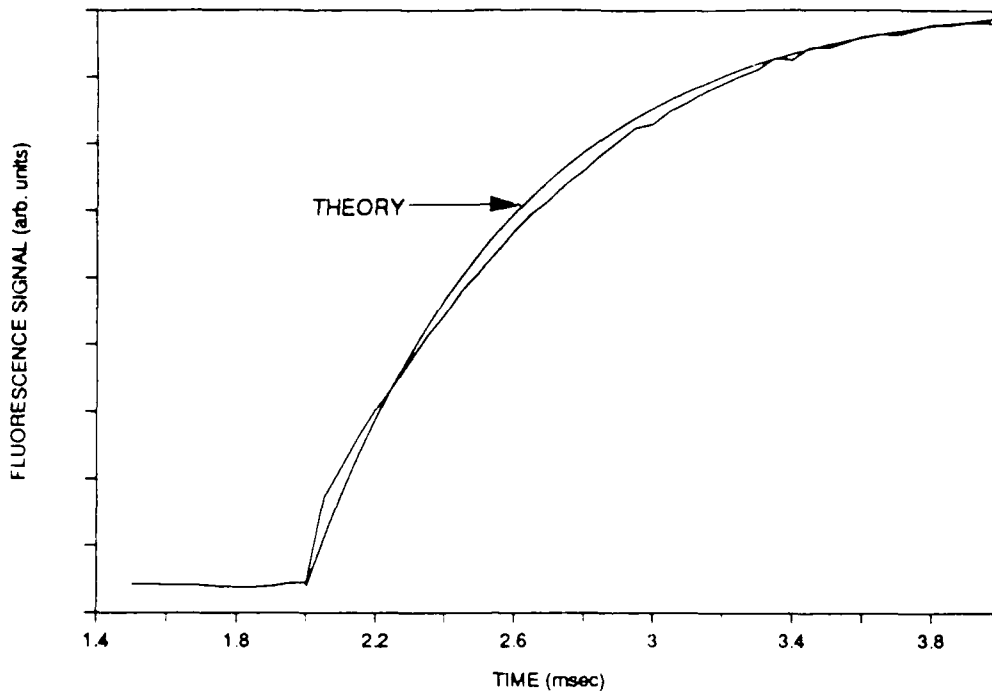
23

Figure 25. Buildup of 1600-nm emission, with model.

The decay of 1600-nm emission is well-characterized by a single decay time of 5.1 msec, as shown in Fig. 26.
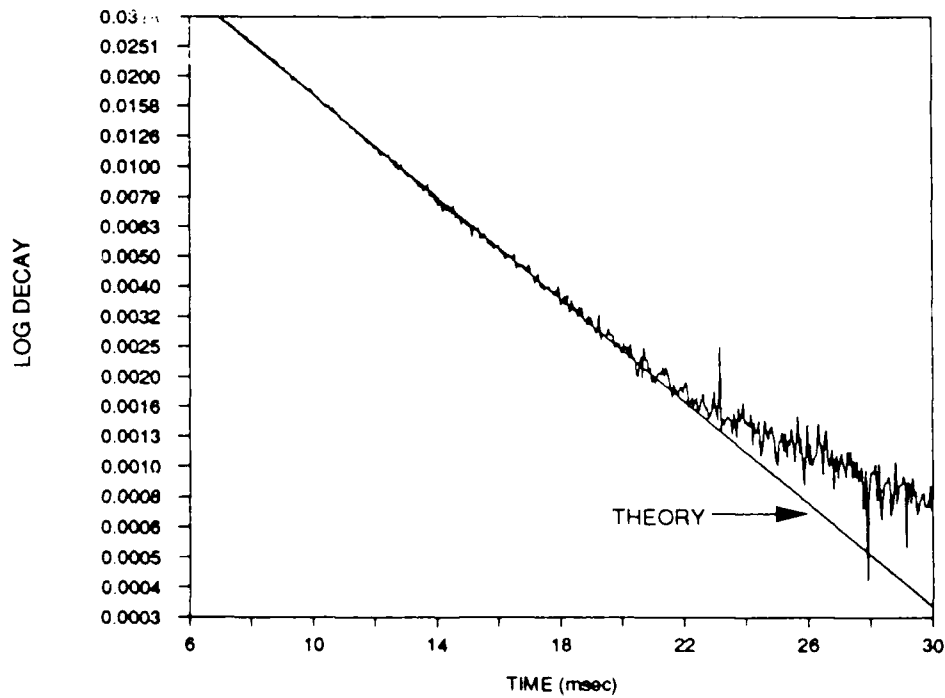

Figure 26. Decay of 1600-nm emission, with model.

3.4.3 Cr³⁺ Decay

The decay of Cr³⁺ emission at 750 nm was observed with the use of a 450-nm excitation source. From the excitation-spectra and Er³⁺-emission buildup data we would expect that the Cr³⁺ lifetime would be reduced considerably from the 145-microsecond value observed in YSGG crystals singly doped with Cr³⁺. The decay data shown in Fig. 27 confirms this, showing that the initial decay is approximated by a time constant of 0.85 microseconds. Since the transfer rate of excitation from Cr³⁺ to Er³⁺ ions depends on the Cr-Er ion spacing, which varies from one Cr ion to another, we would not expect that the Cr³⁺ decay would be at a single rate. Therefore, the poor fit of the decay to a single rate model is not unexpected. Based on the decay data, if we assume that all of the reduction in Cr³⁺ lifetime is due to transfer to Er³⁺ ions, we can conclude that the transfer of excitation from Cr³⁺ to Er³⁺ ions is essentially 100% efficient.
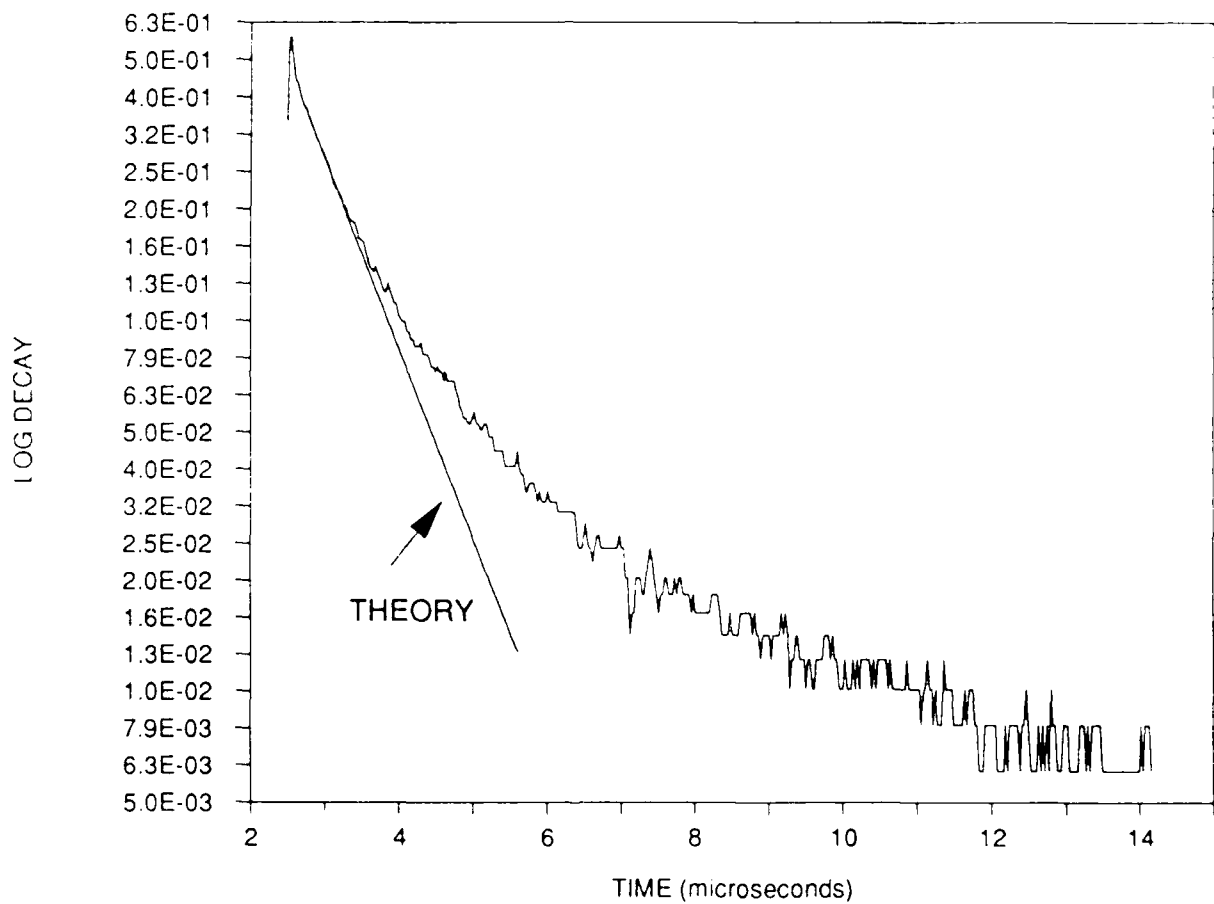

Figure 27. Decay of Cr³⁺ emission, with model.

4 Laser Data

The laser rod fabricated from the Er,Cr:YSGG boule was optically pumped by a 4-mm bore-diameter by 63-mm discharge-length xenon flashlamp in a close-coupled, silvered, elliptical pump cavity. The flashlamp was simmered and driven by a conventional, single-mesh LC discharge circuit. The flat and parallel laser rod ends were uncoated, as we had discovered from previous research that antireflection coatings for the 2800-nm region invariably were lossy due to the presence of entrapped water.

4.1 Input-Output Data

We measured the laser threshold for different lamp pulsewidths. The laser cavity consisted of a 90%-reflecting flat output mirror and a highly-reflecting 10-m concave mirror spaced 36 cm apart, with the laser rod centered between the mirrors. Table 4 lists the observed lamp-energy inputs at threshold for a range of (full-width at half maximum) pulsewidths, along with the values of the discharge capacitor and inductor.

Table 4. Er,Cr:YSGG laser threshold vs pump pulsewidth.

Pulsewidth (microseconds)	Threshold Energy (Joules)	Capacitance (microfarads)	Inductance (microhenries)
44	8.4	10	40
70	5.4	25	40
90	5.1	35	40
110	5.1	50	40
150	6.3	100	40
220	7.9	210	20

Our experience with other 2800-nm-region Er lasers, in YAG and LiYF$_4$ (YLF) host crystals, showed that laser thresholds under conditions similar to those for the Er,Cr:YSGG laser were considerably higher, in the range 30-45 Joules.

Figure 28 presents multimode output energy as a function of lamp input energy for two different output mirror reflectivities, 70 and 90%. The discharge network was a 210-microfarad capacitor and a 40-microhenry inductor and the pulse repetition rate was 1 Hz. Slope efficiencies were approximately 1% in both cases. At the highest energy output the laser beam divergence was approximately 5 mrad, or 9-times diffraction limit. We placed an aperture in the laser cavity to limit the number of transverse modes in operation and were able to obtain 120 mJ of energy in a diffraction-limited beam and 200 mJ of output from a beam with less than twice the diffraction-limited divergence.

The average power output of the Er,Cr:YSGG laser as a function of pulse repetition rate, for different pump energies, appears in Fig. 29. The discharge network was the same as used for the data of Fig. 28 and the output coupler was 90% reflective. At high pump energies there is an evident reduction in the energy per pulse for increasing repetition rate.

The slope efficiency of the Er,Cr:YSGG laser is similar to our data for Er:YAG systems (which employ 6.3-mm-diameter by 100-mm-long laser rods) and higher than efficiencies observed to date with Er:YLF. The reduction in pulse energy at high repetition rates, presumably connected with thermal effects in the laser rod, is much less than that observed in Er:YAG or Er:YLF systems at the same output energies.
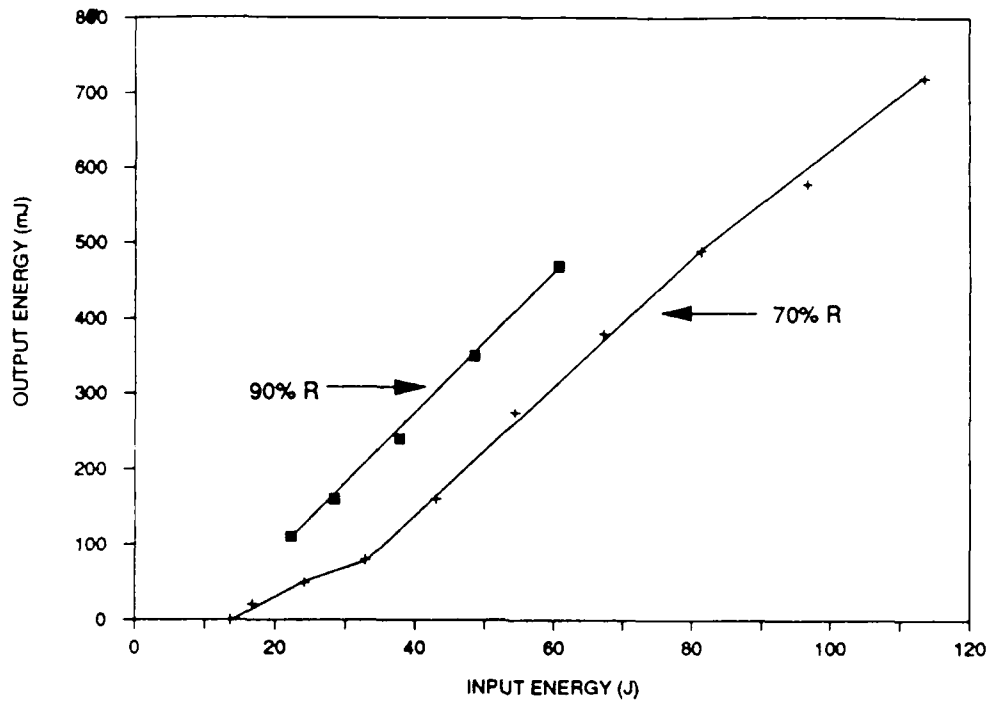
Figure 28. Er,Cr:YSGG laser output energy vs input energy for two different output-mirror transmissions.
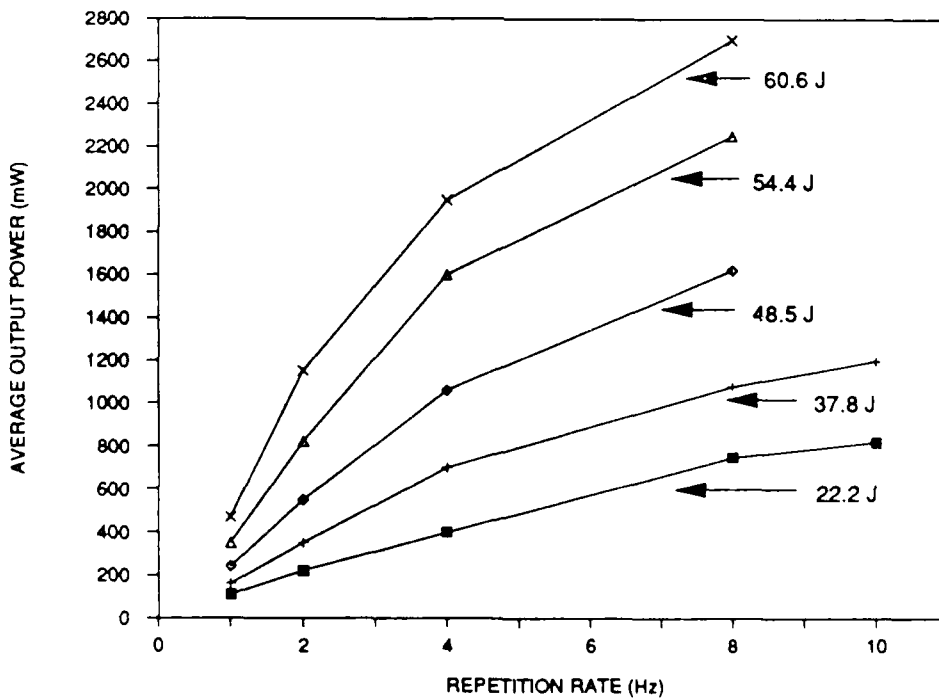

Figure 29. Er,Cr:YSGG laser average-power output as a function of repetition rate, for different pump energies

27

4.2 Temporal Data

The output of the laser near threshold was a single short (microsecond range) pulse, occurring near the end of the lamp pulse. At higher pumping levels the output appeared as a series of short pulses (or "spikes"), characteristic of laser systems having upper-state lifetimes much longer than the laser cavity lifetime, and pumped with pulses shorter than or equivalent to the upper-state lifetime. Figure 30 is an oscilloscope photograph of the combined outputs of the Er,Cr:YSGG laser and the flashlamp pump pulse, showing the timing of the laser output with respect to the pump. The laser output energy was 15 mJ, with the laser pumped at twice threshold and operating on a single transverse mode. A series of distinct pulses is evident on the smooth envelope of the flashlamp pulse. With the laser operating on a number of transverse modes, well above threshold, the pulses appear at a higher rate, as shown in Fig. 31. The data is for a multimode output energy of 580 mJ, with the laser pumped at 7 times over threshold.

Fig. 30. Output pulse of Er,Cr:YSGG laser at   Fig. 31. Output pulse Er,Cr:YSGG laser at
15-mJ level, superimposed on flashlamp pulse.   580-mJ level, superimposed on flashlamp pulse.

4.3 Wavelength Measurement

We measured the output wavelength of the Er,Cr:YSGG laser by the use of a 0.68-m grating spectrometer, the calibration of which had been checked with a mercury lamp. The wavelength was 2740 nm, which corresponds (from Table 3) to a transitions between the 4th level of the $^4I_{11/2}$ manifold and the 4th level of the $^4I_{13/2}$ manifold.

5 Summary of Technical Results

We have carried out a study of the spectroscopic and laser properties of Er,Cr:YSGG. We measured the absorption spectra of a crystal over the range 300-1700 nm and the emission spectra of Er^{3+} ions in the 1600 and 2800-nm wavelength regions. Using that data we have derived a set of energy levels for Er3+ for the lowest four manifolds and have identified the transitions associated with essentially all of lines in the emission spectra. In addition, we have observed the excitation spectra for 1600 and 2800-nm emission in the region from 250-850 nm, and have concluded that nearly all of the excitation absorbed by the Cr^{3+} ions transfers over to the Er^{3+} ions. This conclusion is supported by measurements of the lifetime of the Cr^{3+} emission at 750 nm, 0.85 microseconds, greatly reduced from the lifetime of 145 microseconds observed in Cr:YSGG, and the very rapid buildup of Er^{3+} emission under conditions in which only Cr^{3+} ions are initially excited. Our data on Er^{3+} emission taken with pulsed excitation sources indicates that lifetimes for 1600 and 2800-nm fluorescence bands are 5.1 and 1.4 milliseconds, respectively. A rod of Er,Cr:YSGG has been operated as a laser at 2740 nm, with a flashlamp pumped threshold as low as 5 Joules, slope efficiencies of up to 1%, repetition rates ranging up to 10 Hz and an average power output of 2.7 Watts. The performance of the Er,Cr:YSGG laser is generally superior to other 2800-nm-wavelength Er-doped laser crystals.

6 References

1. E.V. Zharikov et al, Sov. J. Quantum Electron. **13**, 82 (1983).
2. P.F. Moulton, Digest of Technical Papers, CLEO '84, 19-22 June, 1984, OSA/IEEE, Anaheim, CA, Paper WA2.
3. E. Reed, IEEE J. Quantum Electron. **QE-21**, 1625 (1985).
4. Z.J. Kiss and R.C. Duncan, Appl. Phys. Lett. **5**, 200 (1964).
5. P.F. Moulton, 'Paramagnetic-Ion Crystalline Lasers', in Handbook Series on Laser Science and Technology, Volume 1: Lasers in All Media, M.J. Weber ed., (CRC Press, Boca Raton, Florida) pp. 21-146.
6. W.F. Krupke, Lawrence Livermore Laboratory, private communication.
7. E.V. Zharikov, V.V. Osiko, A.M. Prokhorov and I.A. Shcherbakov, Inorg. Mat. **48**, 81 (1984).
8. E.V. Zharikov et al, Sov. J. Quantum Electron. **16**, 145 (1986).
9. E.W. Duczynski, G. Huber, V.G. Ostroumov and I.A. Shcherbakov, Appl. Phys. Lett. **48**, 1562 (1986).
10. I.A. Shcherbakov, Digest of Technical Papers, CLEO '86, 9-13 June, 1986, OSA/IEEE, San Francisco, CA, Paper WC3.
11. A.A. Kaminskii et al, Phys. Stat. Solidi (a) **39**, 541 (1977).
12. V.I. Zhekov, V.A. Lobachev, T.M. Murina and A.M. Prokhorov, Sov. J. Quantum Electron. **13**, 1235 (1983).

7 Personnel

Dr. Peter F. Moulton served as Principal Investigator of the effort. Assisting him in the research were Glen A. Rines and Jeffrey G. Manni.
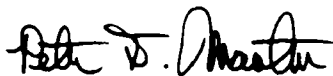
8 Interactions

A paper entitled "Characteristics of 2.9-micron Laser Operation in Er-doped Crystals" by J.G. Manni, G.A. Rines and P.F. Moulton was presented at the CLEO'87 Conference, in Baltimore, MD on April 30, 1987. The paper, given by J.G. Manni, included the Er,Cr:YSGG laser results discussed above. An Abstract and Summary of the paper are included as Appendix A.

9 Certification of Technical Data Conformity

The Contractor,   **Schwartz Electro-Optics, Inc.**   , hereby certifies that, to the best of its
knowledge and belief, the technical data delivered herewith under contract No.
F49620-86-C-0074 is complete, accurate, and complies with
all requirements of the contract.

5 JUNE 1987   **Dr. Peter F. Moulton, Vice President**
Date   Name and Title of Certifying Official

10 Appendix A

Characteristics of 2.9-micron Laser Operation in Er-doped Crystals

J.G. Manni, G.A. Rines and P.F. Moulton
Schwartz Electro-Optics, Inc.
45 Winthrop Street Concord, Massachusetts 01742
(617) 371-2299

ABSTRACT

The performance of the crystals Er:YAG, Er:YLF and Er:Cr:YSGG as flashlamp-pumped 2.9-micron lasers has been examined. Output energies of 1.2 Joules, slope efficiencies of 1.4% and thresholds as low as 5 Joules have been observed

Characteristics of 2.9-micron Laser Operation in Er-doped Crystals

J.G. Manni, G.A. Rines and P.F. Moulton
Schwartz Electro-Optics, Inc.
45 Winthrop Street Concord, Massachusetts 01742
(617) 371-2299

The 2.9-micron laser transition of the Er^{3+} ion in a variety of host crystals has been studied for more than a decade. Recent development of Er lasers has been motivated by potential medical applications. In this paper we present results on a study of three different 2.9-micron Er-doped systems, Er:YAG, Er:YLF and Er:Cr:YSGG.

The Er^{3+} laser transition in question, from the $^4I_{11/2}$ to the $^4I_{13/2}$ states, is similar to the 1.06-micron transition of the Nd^{3+} ion in being 4-level in nature, but the similarity ends at that point. The Er-laser terminal-level manifold has a longer lifetime than that of the upper level, a condition which to date has prevented attainment of cw operation. Not all the excitation into high-lying Er levels decays down to the upper laser level (some feeds the terminal level) and at high pumping rates there is some evidence that pumping transitions can originate on the terminal level. The fluorescence quantum efficiency is much less than unity and is strongly dependent on the host crystal. Finally, strong interactions between pairs of excited Er^{3+} ions (cross relaxation) can occur and provide excitation-dependent decay channels as well as means for population of the upper level. Our experimental studies have been aimed at providing data to test various models of Er kinetics and have characterized flashlamp-pumped lasers in terms of threshold, slope efficiency and temporal behavior under normal-mode and q-switched conditions, with variables of output-mirror transmission, pulse repetition rate, flashlamp pulse duration and, in some cases, Er doping level. Rate-equation models to fit the data are currently under development.

Figure 1 shows energy input-output curves for the three materials studied. The Er doping levels for the YAG, YLF and YSGG rods were at 50, 5 and 30 percent, respectively, and the YSGG crystal was co-doped with 2% Cr^{3+}. All laser rods were 6.3-mm in diameter (the YAG and YLF rods were 100 mm in length while the YSGG rod was 75 mm long) and the output mirror had 10% transmission. Er:YAG exhibits a relatively high slope efficiency (up to 1.4% in some of our experiments) but also has a high threshold, primarily because the upper-state lifetime of 100 microseconds (primarily nonradiative) is the shortest of the three materials. We have generated up to 1.2 Joules of output from Er:YAG at a pump energies of 220 Joules. The Er:YLF rod shows a comparatively low slope efficiency, which we believe is due to the low level of doping. Experiments are planned with laser rods having a much higher Er level, in order to see if the Er:YLF performance can be improved. The YLF host crystal is of interest because of the long (4 msec) upper-state lifetime[1] and the lack of thermal lensing[2], important for systems requiring a combination of high average powers and good beam quality.

Results with the Er:Cr:YSGG rod are most encouraging, combining a low threshold with a high slope efficiency. The crystal is the most recently discovered of the three studied (the first demonstration of laser action was reported by Shcherbakov[3] last year) and the data was taken with material from the first commercially (Airtron) grown boule. The good performance of the crystal is due to the 1-msec-long upper-state lifetime as well as the effects of Cr^{3+} sensitization. Thresholds as low as 5 Joules have been observed with optimal pump pulsewidths.

We have also carried out q-switching experiments, generating up to 100 mJ in a 200-ns-wide pulse from an Er:YAG system, and details of the q-switching results will be reported.

References:

1. E.P. Chicklis, L. Esterowitz, R. Allen and M. Kruer, Proceedings of Lasers '78, Orlando, Florida, 1978.
2. J.E. Murray, IEEE J. Quantum Electron. **QE-19**, 488 (1983).
3. I.A. Shcherbakov, Digest of Technical Papers, CLEO '86, San Francisco, California, June 1986, p. 155.

Figure caption:

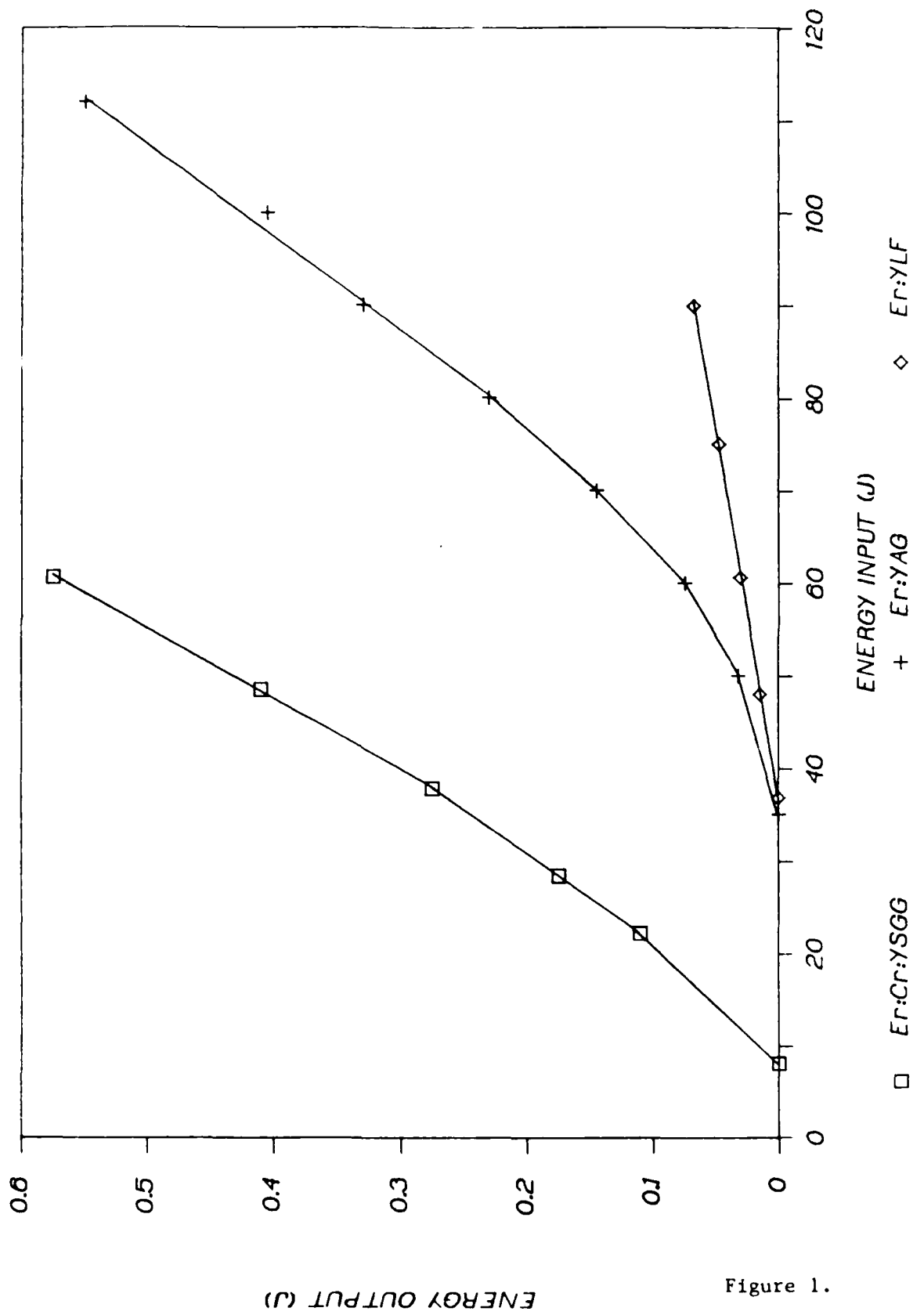Input-output energy curves at 2.9-microns wavelength for 3 different Er-doped crystals.

ENERGY OUTPUT (J)

ENERGY INPUT (J)   + Er:YAG   ◊ Er:YLF

□ Er:Cr:YSGG

Figure 1.

END

DATE
FILMED

DEC.
1987